The response of permafrost to inundation below a rapidly eroding Arctic island

Mehriban Aliyeva[1, 2], Michael Angelopoulos[1, 3], Julia Boike[1, 4], Moritz Langer[1, 2], Frederieke Miesner[1, 5], Scott Dallimore[6], Dustin Whalen[7], Lukas U. Arenson[8], and Pier Paul Overduin[1]

[1]Permafrost Section, Alfred Wegener Institute Helmholtz Centre for Polar and Marine Research, Potsdam, Germany
[2]Department of Earth Sciences, Vrije Universiteit Amsterdam, Amsterdam, The Netherlands
[3]Chair of Landslide Research, Technical University of Munich, Munich, Germany
[4]Department of Geography, Humboldt Universität zu Berlin, Berlin, Germany
[5]Department of Geosciences, University of Oslo, Norway
[6]Natural Resources Canada, Dartmouth, NS, Canada
[7]Natural Resources Canada, Sidney, BC, Canada
[8]BGC Engineering, Vancouver, BC, Canada

Correspondence: Mehriban Aliyeva (mehriban.aliyeva@awi.de)

Abstract.

Tuktoyaktuk Island acts as a natural breakwater, protecting the harbour and townsite of Tuktoyaktuk — an Arctic community that has faced coastal retreat and its consequences for decades. Increasing storm activity, coupled with a longer open-water season, is rapidly eroding the island's shoreline and inundating the underlying permafrost. Once inundated, permafrost warms and degrades, further undermining coastal stability. This study investigates both short and long-term permafrost changes during the transition from terrestrial to subsea. We used Electrical Resistivity Tomography (ERT) to estimate the depth of the ice-bearing subsea permafrost table (IBPT), capturing the short-term response. By integrating subsurface resistivity data with historical shoreline positions and thermal modelling, we also gain insights into long-term degradation patterns. Our results reveal a distinct contrast in IBPT shape between the ocean-facing and harbour-facing nearshore zones, indicating the influence of coastal erosion rates and corresponding inundation times. Additionally, small-scale variations appear linked to local geological differences. In the long term, changes in subsurface composition point to more rapid ice loss within the permafrost than can be explained by the temperature gradient caused by inundation alone. We suggest that subsea permafrost north of the island is more degraded than previously thought, potentially accelerating the projected breach, which was last estimated to occur by 2044. These findings enhance our understanding of subsurface processes driven by coastal retreat and offer valuable insights that can inform engineering strategies to fortify the island.

1 Introduction

Arctic coasts are vulnerable to climate change due to the presence of ground ice, which facilitates thermal abrasion - a process combining wave action and ground ice melt that accelerates erosion (Aré, 1988). This vulnerability is heightened by excess ice in coastal cliffs and the formation of thermokarst features, which further destabilize the coastal zone (Lantuit et al., 2013).

20 Consequently, many Arctic coasts are eroding at rates far exceeding those of temperate regions (Jones et al., 2020), driven by subsea permafrost thaw, subsidence, sea-level rise, and wave-driven erosion (Creel et al., 2024).

Subsea permafrost refers to frozen soil or sediment beneath the seabed that remains below $0\,°C$ year-round. Most subsea permafrost originally formed on land as terrestrial permafrost, which became submerged due to rising sea levels or coastal erosion (Overduin et al., 2012). Once submerged, permafrost is no longer exposed to cold air temperatures but is instead regu-
25 lated by seawater, which acts as a thermal buffer, warming the upper sediment layers and affecting the underlying permafrost (Angelopoulos et al., 2019). Warming and thawing of ice-rich subsea permafrost in the nearshore region deepens the bathymetric profiles, allowing waves to break closer to shore and increasing their erosive potential (Dallimore et al., 1996). In areas with strong erosion, the seasonal formation of bottom-fast ice (BFI) allows for relatively rapid heat loss from the seabed to the atmosphere compared to floating ice zones in winter. However, the brine released from growing sea ice during winter can
30 diffuse or flow into the shallow subsea permafrost and melt ground ice. Under the assumption that the atmosphere-seabed thermal coupling dominates over sea ice brine release in winter, thinner sea ice and increased wave action further accelerate subsea permafrost degradation (Overduin et al., 2012).

Tuktoyaktuk Island, situated on the southern ice-rich coast of the Beaufort Sea to the east of the Mackenzie Delta, provides a critical case study for the above-mentioned processes. Acting as a natural barrier, it protects parts of the Tuktoyaktuk hamlet
35 and harbour from the full fetch of Kugmallit Bay. The hamlet belongs to the Inuvialuit Settlement Region in Canada's Northwest Territories, the traditional territory of the Inuvialuit which faces multiple challenges brought about by climate change, threatening lives, livelihoods, and cultural practices reliant on wildlife resources. Tuktoyaktuk (The Hamlet of Tuktoyaktuk, 2024) has a population of 937 (Statistics Canada, 2022) and has experienced severe coastal erosion for at least decades, facing similar challenges to the other 378 coastal settlements on permafrost (Ramage et al., 2021). Since completion of the Inuvik-
40 Tuktoyaktuk Highway in 2017, Tuktoyaktuk's harbour on the Arctic Ocean coastline has been connected to the Canadian road system. Historical records show that between 1935 and 1971, some areas of town experienced over 100 m of erosion (Rampton and Bouchard, 1975). Despite various shoreline protection measures—including Longard tubes installed in 1976, sandbags used between 1987 and 1993, and monolithic concrete slabs placed in 1998 (Couture et al., 2002; Johnson et al., 2003) — erosion continues to threaten the community. The mean rate of coastal retreat of the southern shore of Kugmallit Bay has been
45 estimated to be $0.34\,\mathrm{m\,yr^{-1}}$ for the time period of 1974-2000 (Solomon, 2005; Hynes et al., 2014; Whalen et al., 2022). Erosion rates at Tuktoyaktuk are some of the highest in the region with up to $2\,\mathrm{m\,yr^{-1}}$, and singular events exceeding $10\,\mathrm{m\,yr^{-1}}$ (Solomon, 2005; Hynes et al., 2014; Whalen et al., 2022). Tuktoyaktuk Island, a western Canadian Arctic erosion hotspot, is projected to be breached by 2044 or sooner. If left unmitigated, the Tuktoyaktuk community will be vulnerable to increased wave action (Whalen et al., 2022). As part of an ongoing shoreline fortification project, revetments composed of armour stone,
50 insulation, and geotextile are being placed along the northern shore of the island and the ocean-facing parts of the Tuktoyaktuk Peninsula in 2024 (Scott et al., 2022; Arenson et al., 2025).

The rapid retreat of Tuktoyaktuk Island accelerates the transition from terrestrial to submarine permafrost as inundation progresses. The island, thus, provides a unique case to study this dynamic transition zone. Previous studies have explored the temporal evolution of subsea permafrost by examining sections extending seaward from the shoreline for several hundred

meters, which provide a relatively reliable timeline of inundation (Aré, 2003). This approach, combined with ERT, has been applied in multiple Arctic regions, such as Barrow Peninsula (Overduin et al., 2012), Kaktovik Lagoon (Pedrazas et al., 2020), and Drew Point (Arboleda-Zapata et al., 2022) on the Alaskan Beaufort coast, as well as Muostakh Island (Overduin et al., 2016), Buor-Khaya Bay (Shakhova et al., 2017), and the Bykovsky Peninsula (Angelopoulos et al., 2021; Arboleda-Zapata et al., 2022) in eastern Siberia. A recent study mapped subsea permafrost around Tuktoyaktuk island, revealing variations in the permafrost table associated with erosion patterns (Erkens et al., 2025), but the nearshore regions (roughly $< 100\,\mathrm{m}$ from the shoreline) remain understudied.

To address this gap, we focus on the terrestrial permafrost directly beneath the island and the subsea permafrost (extending from the shoreline to approximately $100\,\mathrm{m}$ offshore) that have recently experienced, or are currently undergoing, marine submergence. Our objectives are twofold: a) to analyse the short-term and surface-layer responses of permafrost to coastal retreat by inferring the depth and shape of the IBPT using ERT; and b) to examine the longer-term thawed layer and sub-IBPT responses by deciphering compositional changes at depths unaffected by seasonal air temperature fluctuations. This is achieved by integrating resistivity distribution data with historical coastline positions and modelling.

This approach aligns with established methods for monitoring the thermal state of terrestrial permafrost, particularly through observations of active layer thickness (ALT) and the depth of zero annual amplitude (DZAA) — the depth below which permafrost temperatures remain stable throughout the year.

2 Methods

2.1 Study Region

Tuktoyaktuk Island is part of a broader, northeast-oriented Tuktoyaktuk Peninsula located on the southeastern coast of the Beaufort Sea, to the east of the Mackenzie Delta. The peninsula belongs to the Tuktoyaktuk Coastlands division of Arctic Coastal Plain (Bostock, 1970). These are characterized by unconsolidated sediments consisting of Pleistocene glacial till, outwash, and aeolian sediments with some areas with extensive Holocene lacustrine basins (Rampton, 1988; Dallimore et al., 1996). This region was glaciated, covered by the Laurentide Ice Sheet during the Toker Point Stade (Rampton, 1988; Bateman and Murton, 2006) of the Late Wisconsinan, between 22 and 16 ka (Murton et al., 2007), with permafrost predating glaciation due to the exposure of lowlands during sea level fall prior to the Last Glacial Maximum (Murton et al., 2004; Forbes et al., 2014). Postglacial thermokarst processes and marine transgression from Holocene sea level rise of $\approx 70\,\mathrm{m}$ (Hill et al., 1985) have shaped the landforms, including ice-rich cliffs, breached thermokarst-lake estuaries, ice-wedge polygons, and pingos (Harper, 1990; Forbes et al., 2014).

This combination of glacial and transgressive history has resulted in continuous permafrost today up to $400\,\mathrm{m}$ in thickness in the Tuktoyaktuk region (Hu et al., 2013). The climate is marked by long cold winters lasting for up to eight months and brief, cool summers, primarily influenced by the lingering presence of sea ice in early summer (Burn, 2002). The mean annual air temperature for the period of 1995-2024 recorded at Tuktoyaktuk is $-8.4\,^{\circ}\mathrm{C}$, with mean Thawing and Freezing Degree Days (TDD and FDD) of 954 and 3828 degree-days, respectively (Environment and Climate Change Canada, 2025). The

annual mean ground surface temperature in Tuktoyaktuk is around $-7\,°C$ and has warmed by about $2\,°C$ since the 1970s
(Kokelj et al., 2017). This is consistent with observations of near pan-Arctic permafrost warming (Biskaborn et al., 2019).
Ground ice in the form of massive ice and ice lenses is ubiquitous throughout this area (Rampton, 1988). Southern Beaufort
Sea surface sea temperatures (SST) reached $7\,°C$ in August 2024, exceeding the 1991–2020 August mean by 1–$4\,°C$ in line by
the Arctic Ocean warming observed in the past decades (Timmermans and Labe, 2024). Sea level in the region is driven by sea
level rise, storm surges and to a lesser degree tidal variability (Harper, 1990; Forbes et al., 2014). The coast remains ice-free
for 4 to 5 months annually (Forbes et al., 2014), during which storm surges and waves, primarily from the northwest, exert
significant erosive forces (Whalen et al., 2022). Historical accounts and driftwood surveys indicate storm surges exceeding
$3\,m$ at Tuktoyaktuk (notably in 1944 and 1970), while incomplete tide gauge data show multiple $\geq 2\,m$ events since 2017,
underscoring a persistent risk of high-magnitude surges (MacLeod and Dallimore, 2021).

Tuktoyaktuk Island measures approximately $1550\,m$ in length, with its width varying between 36 and $450\,m$ (Whalen et al.,
2022). It is situated along the northwest-facing coastline of the Tuktoyaktuk Peninsula, a low-relief area with elevations gen-
erally under $5\,m$ (Harper, 1990). The northwestern shore, exposed to dominant wind and wave action, experiences the highest
erosion rates, averaging $1.63\pm0.04\,m\,yr^{-1}$ compared to $0.26\pm0.04\,m\,yr^{-1}$ on the more sheltered, harbor-facing side (Whalen
et al., 2022). The island is primarily composed of glacial sands with inclusions of silt and organic-rich peats, as well as discon-
tinuous bodies of massive ground ice (Whalen et al., 2022).

2.2 Fieldwork

Fieldwork for this study was conducted in July 2023 to investigate the transition from terrestrial to subsea permafrost using
ERT. The ERT method detects resistivity differences of the bulk sediment. This is effective for distinguishing ice-bearing (at
least partially frozen) and ice-free (unfrozen) subsurface material, as the freezing of porewater corresponds to a significant
increase in resistivity (Hauck, 2002; Kneisel et al., 2008; Herring et al., 2023). This method is thus effective for mapping
permafrost extent, but also ice content variations (Yoshikawa et al., 2006). The latter is not limited to terrestrial applications.
In marine environments, ERT is sensitive to the boundary between conductive saline sediments and resistive ice-bonded per-
mafrost (Overduin et al., 2012; Angelopoulos et al., 2020; Arboleda-Zapata et al., 2022; Erkens et al., 2025).

Two amphibious (land-to-sea) profiles (Table 1) were collected on the western and eastern sides of Tuktoyaktuk Island,
aligning with passive seismic data from 2018 and 2021 (Ryberg et al., 2020, 2022; Angelopoulos et al., 2024). Additionally, two
terrestrial ERT profiles (Table 1) were surveyed in the island's center, parallel to the coastline, with their midpoints intersecting
the amphibious lines. These terrestrial surveys offer a baseline of electrical resistivity for colder permafrost, unaffected by
coastal processes or marine submergence. We used an IRIS Syscal Pro (ISP) instrument to collect ERT data, suitable for
both terrestrial and sub-aquatic permafrost studies in fresh and brackish waters. The ISP connects to geoelectric cables with
takeouts that transmit current or measure potential, typically linked to stainless steel electrodes for good contact. On the island
and some nearshore areas, we used $30\,cm$-long electrodes, while offshore we laid cables directly on the seabed, assuming
sufficient contact with the seafloor. Our standard setup consisted of a $5\,m$ electrode separation (along the ground surface),
$200\,V$ transmitter voltage (Tx), $15\,V$ reception voltage, $250\,ms$ injection time, and a Wenner-Schlumberger array configuration,
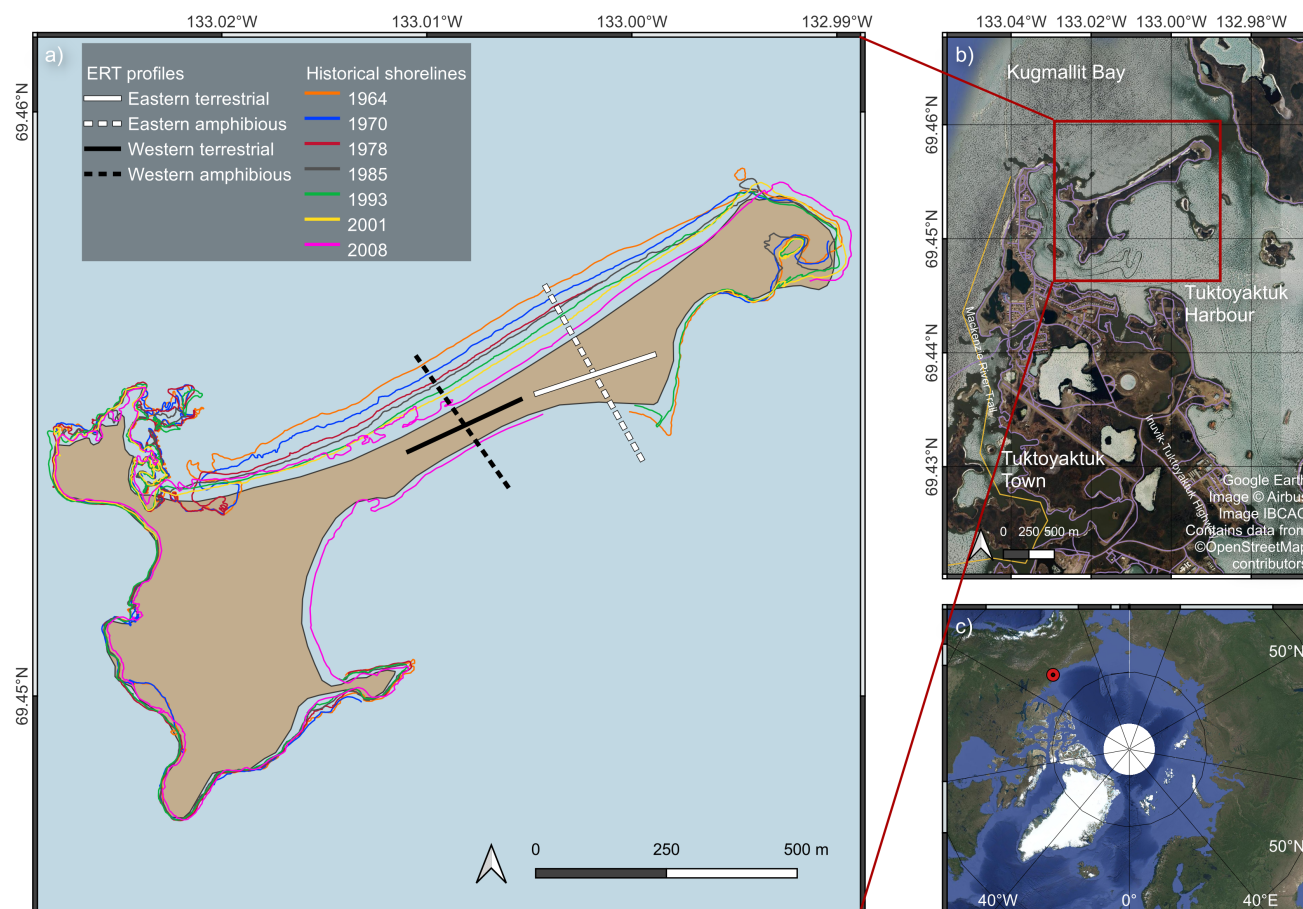
Figure 1. A map of Tuktoyaktuk Island (a) including historical shoreline positions from Hynes et al. (2014) and the ERT profiles used in this study. The upper right panel (b) shows the position of Tuktoyaktuk Island northeast of the hamlet and sheltering the harbour.

which balances spatial resolution and depth penetration. The ISP adjusted Tx for poor contact and used 4–8 stacks with a 5% standard deviation quality threshold. We applied data quality filtering by assigning flags to data points with negative or null apparent resistivities, anomalously low current injection intensity (<1 mA), and Tx voltage failure.

125   Profile locations were georeferenced using a Garmin GPSMAP 64st handheld device, usually at profile ends on land and at one end of each profile on water from the boat used for cable deployment, intersecting historical shoreline positions (Hynes et al., 2014) and Geological Survey of Canada (GSC) borehole locations (Boike and Dallimore, 2019).

For all terrestrial profiles and the land sections of amphibious surveys, active layer measurements were taken at each electrode position using a <1 m-long permafrost probe. Water temperature and conductivity/resistivity were measured using an
130   AML Oceanography™ CTD in profiles north and south of the island throughout the field campaign. Near-bottom water tem-

Profile Type	Location	Date	Electrodes (Quadrupoles)	Segments	Survey Length (m)
Amphibious	Eastern	18–19 July 2023	48 (565)	5	375
	Western	23 July 2023	48 (565)	2	300
Terrestrial	Eastern	19 July 2023	48 (565)	1	235
	Western	24 July 2023	48 (565)	1	235

Table 1. Summary of ERT profiles collected in July 2023, detailed descriptions and raw data was published in (cite report).

perature and conductivity were obtained from a mooring station in Kugmallit Bay, which were measured using Hobo Onset data loggers attached to anchor sacks. A temperature offset at $0\,°C$ in a distilled water ice bath was measured for both electrical conductivity meters of $-0.1\,°C$. Measurements were made at 1 hour intervals for one year (from July 22, 17:00, 2023 to July 22, 17:00, 2024; UTC time). A water density of $1010\,\mathrm{kg\,m^{-3}}$ for brackish water was used to convert measured pressures
135 to water depths, using barometric pressure from the Tuktoyaktuk meteorological station. Land topography at each electrode position was recorded with an Abney Clinometer, while submerged electrode depths were assigned using a bathymetry map interpolated from CTD and Garmin echosounder data, as well as water depths associated with passive seismic measurements taken in 2018 (Ryberg et al., 2020). We did not account for tidal corrections to water levels prior to interpolation.

In September 2021, sediment temperatures over the top $1\,m$ to $1.25\,m$ of the sediment profile were measured with a $1.5\,m$
140 lance at seven locations near the eastern amphibious profile's nearshore section —- four on the southern side and three on the northern side. Using the temperature-depth profiles from these measurements (Miesner et al., 2022, 2024), we extrapolated the temperature curves to greater depths by fitting a second-degree polynomial to the last five data points for each location (Fig. 5).

2.3 Analysis

145 To determine the true subsurface resistivity based on the measured resistances, we inverted the data using `pyGIMLI`, an open-source package for geophysical modelling and inversion (Rücker et al., 2017). We created an error model based on the standard deviation of measurement stacks for each data point and added a minimum 2% error to all points to account for cases where the standard deviation was zero. We excluded the data points where the error exceeded 5% from the inversion to reduce complexity. The geometric factor (to convert resistance to apparent resistivity) was calculated based on the estimated
150 topography and interpolated bathymetry of the terrain. We used unstructured triangular forward meshes and refined them by adding two equidistant nodes between each electrode pair and adjusting the minimal cell size to $25\,\mathrm{m^2}$.

In practice it is impossible to achieve the true distribution of the subsurface properties due to the ill-posed nature of the inverse problem, whereby the data are finite and small changes may cause large variations in the model (Oldenburg and Li, 2005). In addition to the choice of the correct error model, this instability is addressed through model regularization, which controls the
155 relative weighting between data misfit and model norm. The default `pyGIMLI` inversion method employs a generalized Gauss-Newton approach with flexible regularization, controlled by the regularization parameter λ. Small values of λ yield rough but

accurate models, whereas larger values produce smoother models with reduced data fit (Günther et al., 2006). To determine an optimal λ that balances data fit and model constraints, we plotted the Tikhonov curve (Tikhonov, 1963) — the data misfit as a function of the model norm for varying values of λ. We applied the L-curve method (Hansen and O'Leary, 1993) to identify the optimal λ (Table 2), which corresponds to the elbow of the resulting L-shaped curve. We achieved this with the help of the python package `kneed` (Arvai, 2020) which uses the Kneedle algorithm (Satopaa et al., 2011). The elbow was thereby defined as the point of maximum curvature of the third degree polynomial fitted to the Tikhonov curve. Surface measurements often require anisotropic regularization to reduce penalties on vertical contrasts due to layering and lower resolution (Günther and Rücker, 2018). The `zWeight` parameter in `pyGIMLI` adjusts the relative weight of vertical boundaries in the model (Coscia et al., 2011). In the terrestrial surveys we set the `zWeight` to the default value of 1 to avoid artificial layering beneath the island, given that the active layer depth was shallow (less than one metre) and the permafrost body's resistivity is dominated by ice content rather than any sediment stratification. In the offshore parts of our amphibious surveys we do expect layered structures at depth, but due to the complex nature of the amphibious profiles, we reduced zWeight only modestly, to 0.9.

Constraining water-layer resistivity and depth in the amphibious profiles is important for marine ERT inversions, since they can strongly affect the inverted resistivity and thickness values for underlying sediment layers (Arboleda-Zapata et al., 2022). Numerical simulations show that even a thin water layer can attenuate the magnitude of resistivity anomalies, especially as the water thickness increases (Loke and Lane, 2004). To address this, we used `pyGIMLI`'s regional regularization, which allows for flexible regularization by defining and configuring different parts of the inversion domain. We created custom inversion meshes that included separate regions for water on either side of the island, with water layers defined above the interpolated bathymetry. We assigned resistivity limits to each water region based on the CTD measurements performed on the day of the respective survey.

2.3.1 IBPT Interpolation

We interpolated the IBPT based on the inverted resistivity values. Several studies have derived this transition from unfrozen to frozen using a simple cut-off value or range (Overduin et al., 2012; You et al., 2013; Sherman et al., 2017; Angelopoulos et al., 2019; Pedrazas et al., 2020), others have used contours of sharp resistivity rise (Fortier et al., 1994; Overduin et al., 2016). Picking a specific resistivity threshold can be problematic, especially when the freezing point varies along ERT profiles. (Angelopoulos et al., 2021) employed the maximum rate of change of the natural logarithm of resistivity versus depth, while Erkens et al. (2025) tested various approaches, including defining the unfrozen-frozen transition zone based on layered models and the highest vertical resistivity gradient in linear and logarithmic space for smooth models. We adopted a method similar to the latter, whereby our IBPT was identified as the depth where the first change in the order of magnitude of at least 1 occurs in logarithmic space, with a minimum resistivity of $10\,\Omega\mathrm{m}$. This is supported by laboratory studies on Alaskan hypersaline sediment showing that marine sediment resistivity increases sharply, from under $10\,\Omega\mathrm{m}$ to over $100\,\Omega\mathrm{m}$, when sediments freeze and transition from seawater-saturated to ice-saturated (Overduin et al., 2012). Since our inversions were performed on irregular unstructured meshes, we mapped the resistivity values onto a fine regular grid. We smoothed the resulting permafrost table depth line by applying a locally weighted scatterplot smoothing (LOWESS) with window span of 0.2.

2.3.2 Resistivity changes over time

We used a dataset of digital coastlines derived from georeferenced aerial photography (Hynes et al., 2014) to analyse temporal inundation patterns. From this dataset, we selected only the shorelines covered by the amphibious surveys, further refining our selection to include those that afforded us a more regular temporal spacing. We extracted resistivity-depth profiles at each historical shoreline position for the northern side of both eastern and western amphibious surveys, focusing on 20 m below the seabed, the depth where we assume the amplitude of the air temperatures has little to no effect.

To validate changes in resistivity over time prior to and following inundation, we modelled sediment response to higher water temperatures. For this, we used CryoGrid.jl (Groenke and Nitzbon, 2024; Groenke et al., 2023), a partial implementation of the CryoGrid permafrost model (Westermann et al., 2023) written in julia, which provides a versatile framework for simulating ground thermal dynamics including the phase change of partiality frozen sediments. The applied model version includes process modules of heat and water transport, sediment freezing characteristics, surface energy balance, snow cover, and salt diffusion. Sediment freezing characteristics are provided by the FreezeCurves.jl package, which provides implementations of various soil freezing characteristic curves (Groenke, 2025).

We initialized the model using a ground temperature profile from a $20\,\mathrm{meter}$ borehole on the island. The borehole and the temperature loggers were previously described by Lapham et al. (2020) and Ouellette (2021). We extended the temperature profile by linearly extrapolating the deepest three measurements to estimate temperatures an additional $10\,\mathrm{meter}$ below, thereby representing conditions at $20\,\mathrm{meter}$ beneath the seabed. To represent the uncertainties in the ground and porewater properties, we performed ensemble simulations, varying the porosity and porewater salinity. The soil layers were assigned sediment porosities of 0.4, 0.5 and 0.6, with the baseline of 0.5 corresponding to Lapham et al. (2020). Surface sediments collected by Van Veen grab sampler were silt-dominated (Angelopoulos et al., 2025b). We applied the DallAmico freeze curve for silt (Dall'Amico et al., 2011), and shifted it with a salinity-induced freezing point depression. The salt concentration was set based on the porewater resistivities of $1\,\Omega\,\mathrm{m}$, $10\,\Omega\,\mathrm{m}$ and $100\,\Omega\,\mathrm{m}$, representing a range for typical sea and freshwater resistivities and were translated into salt concentration (specifically, molality) using the TEOS-10 model (IOC et al., 2010). Based on Whalen et al. (2022); Lapham et al. (2020), we assumed the soil column to be predominantly composed of silt, for which we used van Genuchten parameters corresponding to silty soil. We set the lower boundary condition at $1000\,\mathrm{meter}$ depth with a default average geothermal heat flux of $0.053\,\mathrm{W\,m^{-2}}$ and the upper boundary condition as a constant temperature of $2.2\,^{\circ}\mathrm{C}$, representing the mean annual seawater temperature in Kugmallit Bay. We ran our simulations for 59 time steps, corresponding to the 59-year inundation period covered by our amphibious surveys. We expect the effects of the lower boundary condition to be negligible for such short term simulations. The model grid resolution was set to $10\,\mathrm{cm}$.

To compare our modelled results with the inverted resistivities, we used Archie's second law (Archie, 1942). Given the liquid water saturation values provided by the simulations from the freezing characteristic curve, we calculated the corresponding bulk resistivities as

$$R_b = a \cdot R_w \varphi^{-m} S^{-n}, \tag{1}$$

where R_b is the bulk resistivity, R_w is the porewater resistivity, S is the liquid water saturation, and φ is porosity. The parameter a represents tortuosity, m is the cementation exponent, and n is the saturation exponent.

To account for changes in porewater resistivity over time, we dynamically adjusted it based on salt dilution or concentration for each time step. In general, the cementation factor (m) increases as the connectivity of the pore network decreases, with typical values ranging from 1.5 to 2.5 for sandy porous media (Glover, 2010). As the ice content decreases with warming, the liquid water saturation increases, leading to lower pore water conductivity but also a more connective porewater network. This connectivity can push m values up to 2.5–3 (Tiab and Donaldson, 2003). We initialized m at 2 and updated it dynamically at each time step based on the new liquid water saturation values to account for the progressive melting of pore ice. The saturation exponent (n), which is related to the wettability of the ground substrate (typically referred as the wettability of rock), influences how well the pore network remains conductive at low water saturation. In water-wet substrate, a continuous thin film of water along pore walls maintains conductivity, and n typically remains close to 2 (Glover, 2010). Therefore, we used a constant value of $n = 2$ in our calculations.

3 Results

3.1 Subsurface resistivity distribution

Submarine and terrestrial permafrost across the island and nearshore zones exhibited pronounced spatial variability, as determined by ERT. We assessed the quality, fit, and limitations of the data. The four measured profiles yielded inverted geoelectrical resistivities that varied by over four orders of magnitude with depth and laterally, particularly with increasing distance from the island. Inverted electrical resistivity values for the amphibious and terrestrial profiles depicted on Figures 2 and 3 lay in between $2.5\,\Omega\,\mathrm{m}$ and $4.1 \times 10^4\,\Omega\,\mathrm{m}$ (Table 2), indicative of unfrozen and frozen sediments within the profiles.

Profile Name	λ	Inversion χ^2	Inversion RRMS	Mean Resistivity (Ωm)	Min Resistivity (Ωm)	Max Resistivity (Ωm)
Amphibious East	20	3.2	10.3	3.5×10^3	2.6	4.1×10^4
Amphibious West	30	4.4	17.5	2.1×10^3	2.5	2.3×10^4
Terrestrial East	30	2.1	7.2	5.4×10^3	476	2.2×10^4
Terrestrial West	35	4.2	10.5	1.5×10^3	85	5.2×10^3

Table 2. Summary table of inversion results, including the inversion setting, diagnostic measures, and resistivity characteristics for each profile. λ represents optimized regularization parameter chosen for each inversion. The χ^2 value measures the difference between observed and predicted data, normalized by the data error, with values closer to 1 indicating a better fit. The RRMS quantifies the average discrepancy between observed and modelled data.

Inversion diagnostics indicated that the data were fitted within the expected error bounds, with χ^2 values ranging from 2.1 to 4.4. Generally, χ^2 values between 1 and 5 suggest a reliable inversion result with minimal over- or under-fitting (Günther et al., 2006). The relative root-mean-squared error (RRMS) values ranged from 7.2% to 17.5%, reflecting a higher absolute misfit. This discrepancy is likely due to the high variance in the data and uneven error weighting, as some points have substantially larger uncertainties than others, particularly at the steep coastal bluffs. For the amphibious surveys, the combination of land and seabed electrodes in individual quadrupoles, high geometric factors on the bluffs as well as poor contact on them due to dry and loose sediment may have contributed to the observed absolute misfit. Despite this, we were able to achieve a random error-weighted misfit distribution for these profiles (Fig.A3).

Depth of Investigation (DOI) index analysis was performed on all four profiles following the method outlined by Oldenburg and Li (1999) to assess the reliability of the inverted models (Fig.A4 and Fig.A5). In line with the approach suggested by Hilbich et al. (2009) for ice-rich permafrost regions, reference models were used with resistivity values set to one order of magnitude below and above the mean apparent resistivity of the dataset. We chose not to apply a strict DOI cutoff but instead used the DOI index as a guideline to inform our interpretation, where DOI indices closer to 1 indicate low reliability. The results indicate that the eastern amphibious survey exhibited better reliability across the inversion domain, particularly within the first $40\,\mathrm{meter}$. A similar trend was observed for the western amphibious profile, although with reduced reliability. For the terrestrial profiles, the data effectively constrained the model parameters only within the upper 15–25 of the inversion domain. All inverted tomograms were displayed to a depth of 40 m from sea level. While the DOI analysis shows some variation in data reliability across the profiles, this depth was chosen to maintain consistency across all profiles.

The two amphibious profiles exhibited similar subsurface features, with high resistivities of $1 \times 10^4\,\Omega\mathrm{m}$ concentrated beneath the island and its immediate nearshore. These values decreased with distance from the shore, dropping below $10\,\Omega\mathrm{m}$ in some areas. Around the bluff and nearshore areas in both amphibious profiles, the tomograms showed lower resistivity zones of varying sizes, most notably on the northern side of the western amphibious line. Overall, the eastern amphibious profile showed higher inverted resistivity values than the western one (Table 2), with the peak in the terrestrial part which gradually decreased from the northern shore but remained above $10\,\Omega\mathrm{m}$, whereas on the southern side, declined rapidly, reaching a minimum of $2.6\,\Omega\mathrm{m}$. Similarly, the western amphibious profile exhibited high resistivities up to $2.1 \times 10^3\,\Omega\mathrm{m}$ beneath the island, decreasing sharply to values less than $10\,\Omega\mathrm{m}$ on the northern side and more gradually on the southern side, with a minimum of $2.5\,\Omega\mathrm{m}$.

The terrestrial profiles (Fig. 3) displayed less variability in the resistivity values than the amphibious profiles. The top 5 meters of both profiles had resistivities below ($1000\,\Omega\mathrm{m}$, which increased with depth to maximum values around $1 \times 10^4\,\Omega\mathrm{m}$. The western terrestrial profile showed a sharp resistivity drop—by two orders of magnitude below the upper $25\,\mathrm{m}$, while the eastern profile displayed a lateral resistivity decrease from east to west. These decreases with depth correlated with regular patterns in the misfit function and occurred at depths where the DOI index approached 1 (Fig. A5). We conducted 3D modelling to determine if the observed regularities in the misfit and inverted resistivity distributions could be attributed to the proximity of conductive seawater on either side of the terrestrial profiles. We created simplified 3D representations of the island of varying width assigning the bulk of the subsurface with a resistivity of $1000\,\Omega\mathrm{m}$ and the water with $1\,\Omega\mathrm{m}$. We placed virtual electrode arrays, matching the configuration used in the terrestrial profiles, parallel to the shoreline. Inversions of the synthetic data
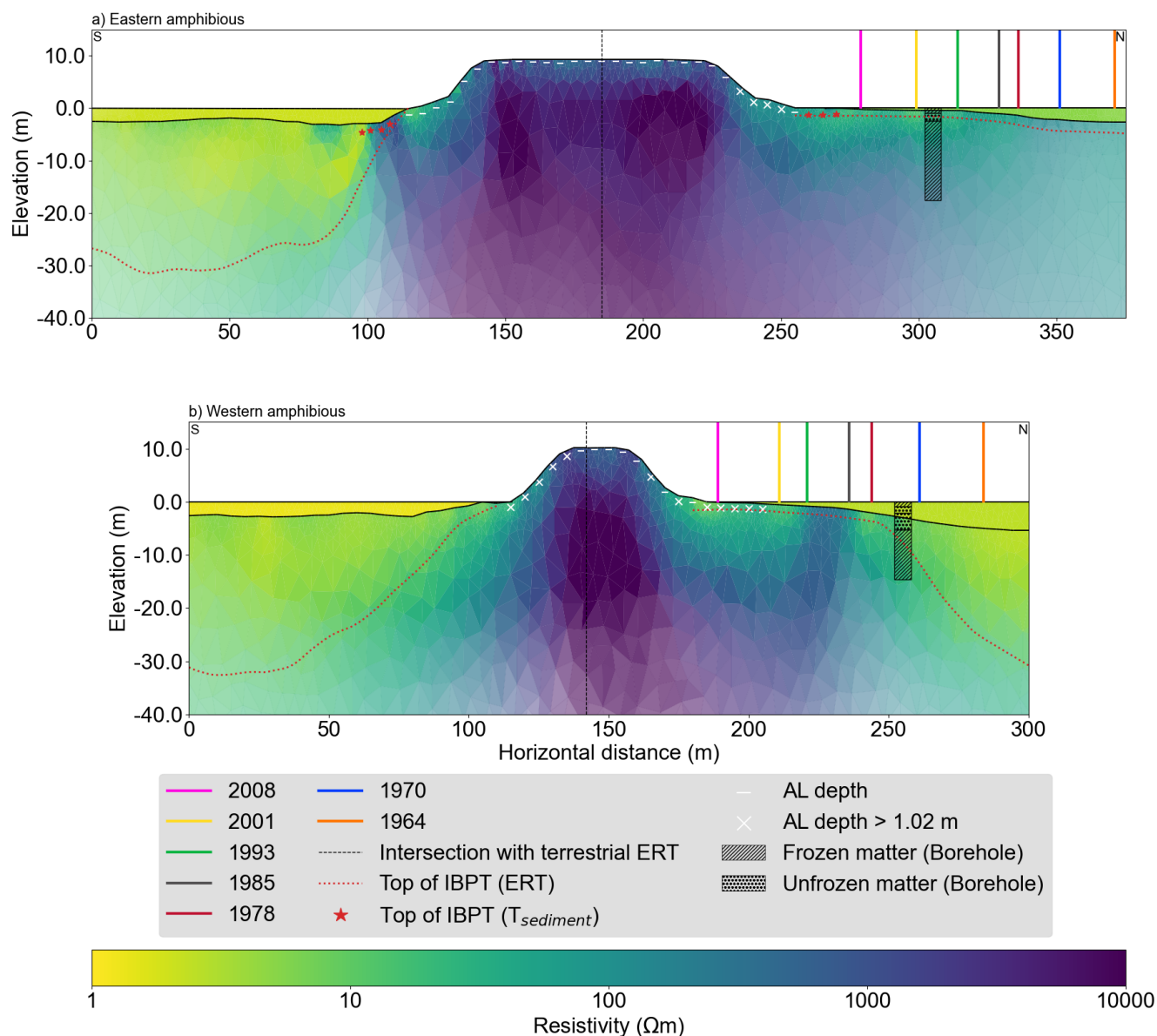
Figure 2. Amphibious ERT profiles along the eastern (a) and western (b) profiles. The opacity of the colours reflects normalized coverage, calculated from sensitivity, response, and resistivity, and scaled to highlight areas above 2% cumulative frequency or below the 0.5 threshold. Intersection positions with the terrestrial profiles are indicated by black dashed lines. ALT is indicated in white dashes and crosses. On the eastern profile, permafrost table depths extrapolated from sediment temperature gradients are indicated by red stars. The determination of frozen and unfrozen sediment in boreholes on the north side of the island are indicated with black hatched borehole profiles. Shoreline positions from 1964 to 2008 (Hynes et al., 2014) are indicated by coloured vertical bars on the north side of the island. On the southern side of the island, shoreline position changed negligibly over the same period. The interpolated and smoothed IBPT is indicated as a red dashed line.
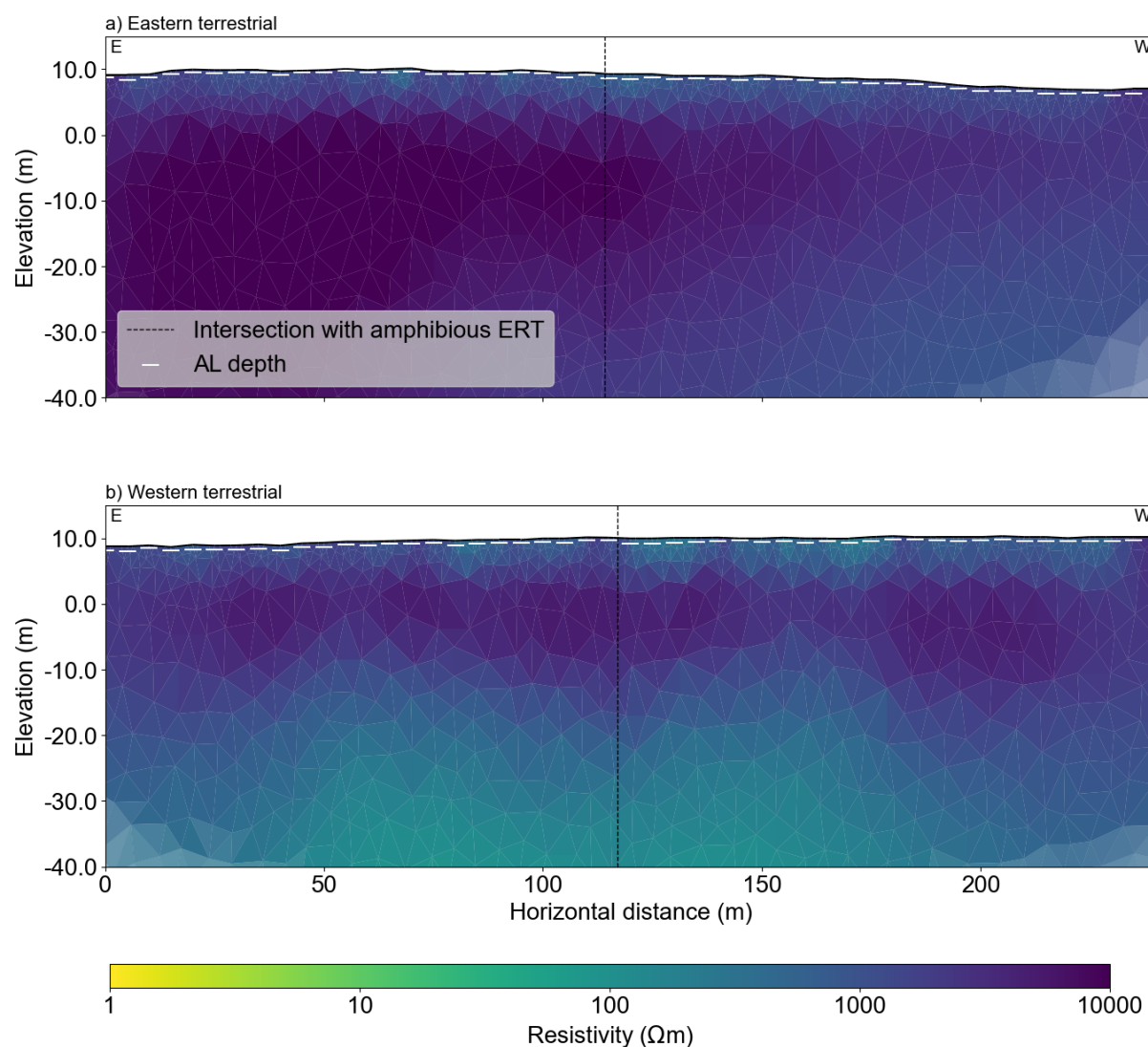
Figure 3. Terrestrial ERT profiles along the eastern (a) and western (b) profiles. Intersection positions with the amphibious profiles are indicated by black dashed lines. ALT is indicated in white dashes. The opacity of the colours reflects normalized coverage, calculated from sensitivity, response, and resistivity, and scaled to highlight areas above 2% cumulative frequency or below the 0.5 threshold.
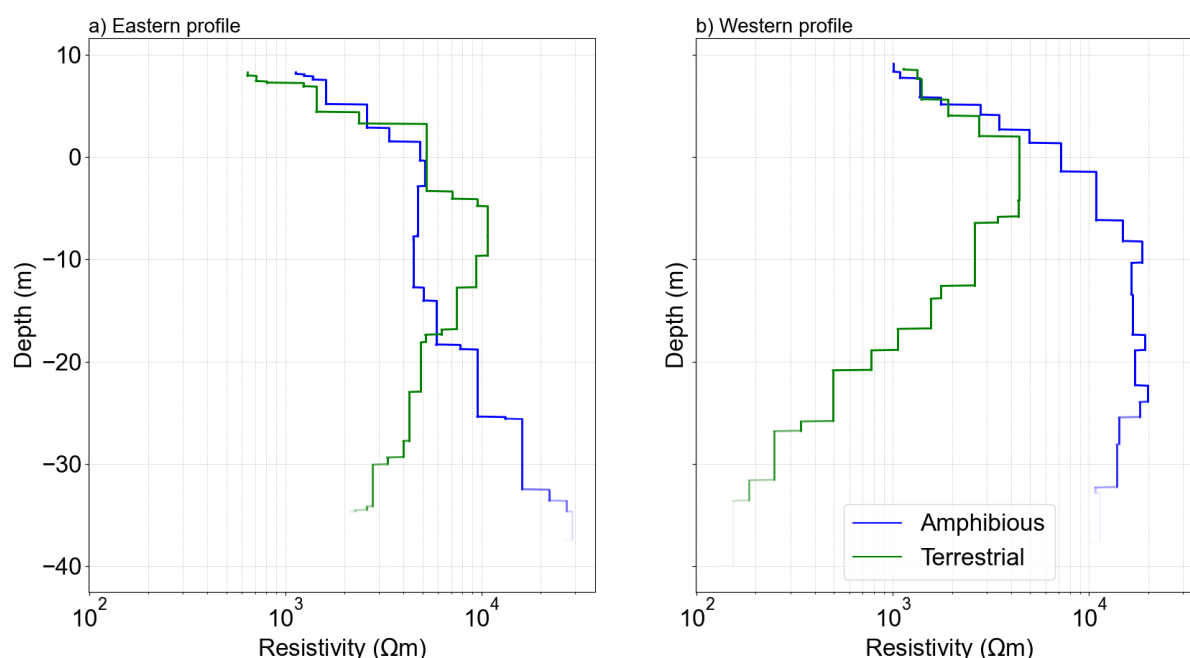
Figure 4. Cross-sectional plots of resistivity versus depth for the eastern (a) and western (b) intersections, with with the x-axis on a logarithmic scale representing the resistivity in Ωm. The colored lines represent data with normalized coverage: blue for amphibious measurements and green for terrestrial measurements. Transparency of the lines corresponds to the degree of coverage, where higher coverage results in more opaque lines.

revealed that a decreasing island width results in a sharp resistivity transition observed at 20 m depth. This model also explains the lateral resistivity decrease observed in the eastern profile as the island narrows (Fig. A2).

280   At the intersection of the eastern amphibious and terrestrial profiles (Fig. 4a), resistivity values closely matched within the first $15\,\mathrm{m}$ before diverging slightly, while remaining within the same order of magnitude. Beyond $30\,\mathrm{m}$, the profiles diverged more significantly. In contrast, at the intersection of the western profiles (Fig. 4b), resistivities began to diverge at a shallower depth, around $8\,\mathrm{m}$. While the divergence at the eastern intersection can be explained by DOI differences, the divergence at the western intersection occurs at a very shallow depth. We attribute this to a high positive misfit in the upper section of the

285   western terrestrial profile, which may be overcompensating for very low resistivities at greater depths, influenced by the 3D effects described above (Fig.A3).

3.2   Temperature regime and permafrost

To characterize the permafrost beneath the island, its rapidly eroding nearshore region, and the offshore, we combined various data including temperature data and ALT measurements collected during our fieldwork. Since our fieldwork was conducted
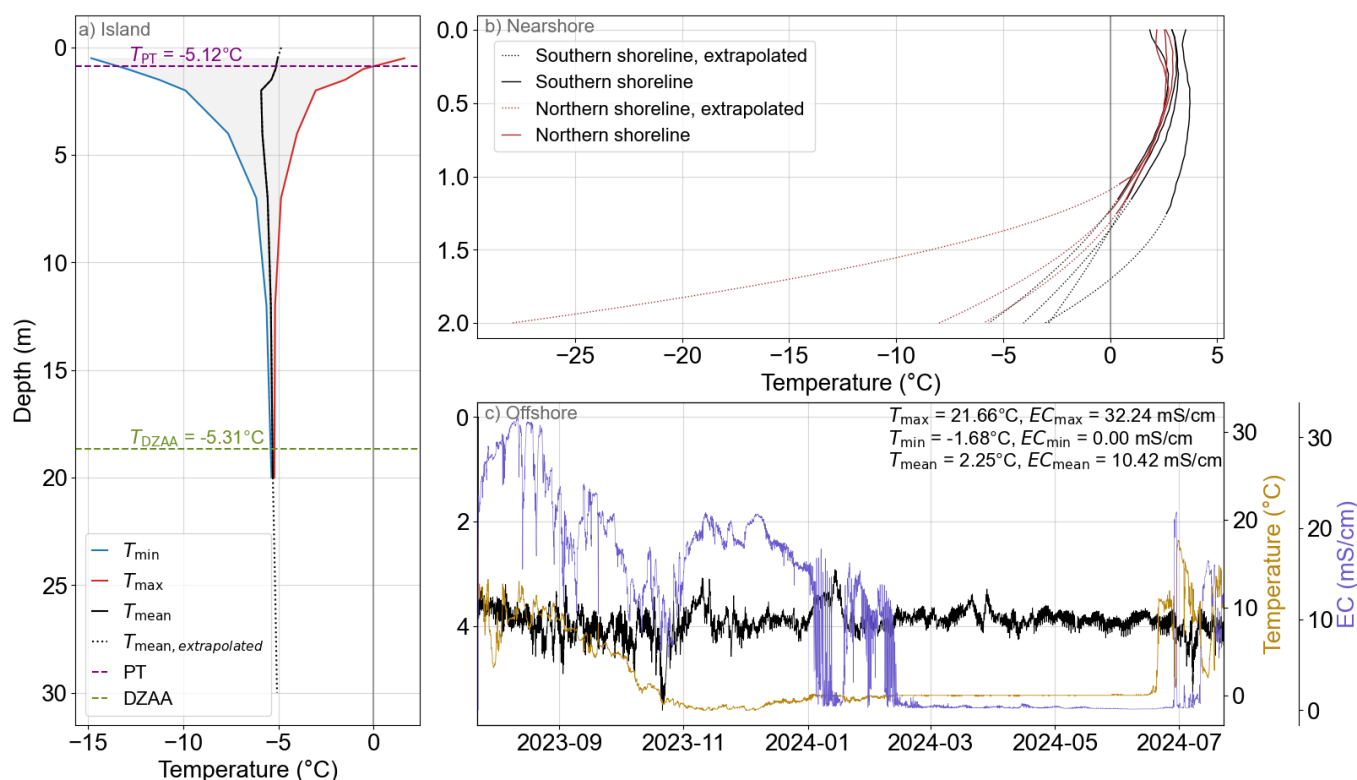
Figure 5. Thermal regime across the shoreface. (a) Borehole temperature data from the island, showing minimum, maximum, and mean annual temperatures for the time period from August 2021 and August 2022 as a function of depth below ground surface. The permafrost table (PT) and Depth of Zero Annual Amplitude (DZAA) are indicated by horizontal dashed lines. The gradient of the mean temperature is extrapolated linearly to 30 m depth. (b) Nearshore sediment temperature profiles from both the northern and southern shorelines, with extrapolated gradients shown as dashed lines, in depth below seafloor. (c) Offshore data, including water depth (black, scale at left in m), and bottom water temperature and electrical conductivity over a one-year period, with annual minimum, mean, and maximum temperatures and electrical conductivities annotated.

290   in July, these ALT measurements are not representative of the end of the thawing season. ALT measurements were taken at every electrode position on land and in shallow water, as indicated by white symbols on Fig. 2 and Fig. 3. The cross symbols mark locations where the ALT exceeded the length of the $1\,\mathrm{m}$ thaw probe. On the island, we were able to record deeper ALT measurements by digging a hole prior to probing, which was not possible on the bluffs. The mean measured ALT was $0.6\,\mathrm{m}$ with its shallowest at $0.2\,\mathrm{m}$ and deepest at $1.5\,\mathrm{m}$ encountered at the bluff area, but with generally low lateral variation across

295   the terrestrial profiles.

The temperature profile of the island's permafrost provides insight into its thermal stability and seasonal variations. We utilized temperature data from a borehole on the island. We focused on the previously unreported, most recent period available (August 2021 to August 2022). The temperatures were recorded at depths of 0.5, 1, 1.5, 2, 4, 7, 12, and 20 m. which we then

extrapolated linearly to the ground surface and an additional $10\,\mathrm{m}$ deeper (Fig. 5a). The mean annual temperature at the ground

300 surface was $-4.8\,^{\circ}\mathrm{C}$, based on the linear extrapolation of the temperature at the shallowest three depths. Based on the borehole temperatures the active layer reached a depth of $0.9\,\mathrm{m}$ on 18th of August 2022, with a mean temperature at the top of the permafrost table equal to $-5.1\,^{\circ}\mathrm{C}$. DZAA was identified at $18.7\,\mathrm{m}$, with a mean annual ground temperature of -5.3°C.

The nearshore permafrost is highly influenced by its proximity to seawater and seasonal changes. Sediment temperatures at the seabed were at least $5\,^{\circ}\mathrm{C}$ higher than ground surface temperatures. The estimated depth of the permafrost table, identified as

305 the depth where each sediment temperature curve crosses $0\,^{\circ}\mathrm{C}$, as illustrated by red stars in Fig. 2a, represented a continuation of the active layer measurements into the nearshore. On the northern side, the permafrost table depth projected from sediment temperature landed in a narrow range of $1.1\,\mathrm{m}$ to $1.3\,\mathrm{m}$. On the southern side, the permafrost table dipped from $1.2\,\mathrm{m}$ at the closest point to the island to $1.7\,\mathrm{m}$ at the farthest point. Both ERT surveys and sediment temperature measurements were conducted along transects oriented toward or crossing two boreholes drilled in 2018 by the GSC as part of their spring nearshore

310 drilling program (Boike and Dallimore, 2019). These boreholes, referenced in the report as Borehole 4 (along the eastern profile) and Borehole 2 (along the western profile), were located $50\,\mathrm{m}$ and $75\,\mathrm{m}$ from the respective shorelines in 2023 (Fig. 2a and Fig. 2b). Borehole 4, situated in shallow water ($\sim0.5\,\mathrm{m}$ depth), encountered frozen sediment at $2.4\,\mathrm{m}$ from sea level. Borehole data indicated that in winter, sea ice extended to the seabed at this location. In contrast, Borehole 2, positioned in deeper water ($\sim3\,\mathrm{m}$ depth), encountered frozen sediment at $5.2\,\mathrm{m}$ from sea level.

315 The offshore environment experiences a distinct thermal regime influenced by water depth, salinity, and seasonal sea ice cover (Aré, 2003). To examine these factors, we recovered temperature and salinity data from a mooring station in Kugmallit Bay, from which annual minimum, mean and maximum values were calculated (Fig 5c). The warm summer water temperatures recorded in the bay corroborated temperatures measured along the CTD profiles in the fieldwork week (Angelopoulos et al., 2025a). , which ranged from $10\,^{\circ}\mathrm{C}$ to $18\,^{\circ}\mathrm{C}$.

320 **3.3 IBPT interpolated from resistivity**

We analysed subsurface resistivity distribution to determine the IBPT in the nearshore areas north and south of Tuktoyaktuk Island (Fig. 2). Along both profiles, the interpolated IBPT on either side of the island aligned with the permafrost table depth measured on the island. The IBPT was relatively shallow, with a gradual dip on the northern side of the eastern profile, consistent with the top of the frozen sediment observed in borehole 2. On the southern side of both surveys, the IBPT dropped steeply

325 from the shore, stabilizing at a depth of around $30\,\mathrm{m}$. On the northern side of the western profile, several ALT measurements taken in shallow water coincided with the location of the interpolated IBPT. These measurements, however, were inconclusive, as the thaw depth probe, which reached a depth of $1\,\mathrm{m}$, suggested the permafrost table lay deeper than this. Two small boreholes drilled for the revetment design at the beach also showed an active layer thickness of about $1.4\,\mathrm{m}$ in 2020. The interpolated IBPT in this region indicated a depth of approximately $2\,\mathrm{m}$. Around $50\,\mathrm{m}$ from the shoreline of the western profile, the IBPT

330 dropped sharply. This steep decline continued until about $100\,\mathrm{m}$ from the shore, where the IBPT stabilized at a depth of around $20\,\mathrm{m}$. At the location corresponding to borehole 2, the IBPT was found at a depth of approximately $8\,\mathrm{m}$ from sea level, which

is about $3\,\mathrm{m}$ deeper than the frozen sediment encountered in the borehole. The resistivity values corresponding to the transition from unfrozen to frozen, based on the position of the IBPT, predominantly ranged from $10\,\Omega\,\mathrm{m}$ to $100\,\Omega\,\mathrm{m}$.

3.4 Resistivity changes over time

335 Historical shoreline positions allow for a temporal analysis of changes in subsurface conditions as the island's northern coastline moved southward and permafrost was inundated. Resistivity-depth profiles at positions extending laterally from the eroding shoreline showed a decrease in resistivity with prolonged inundation time. Along the eastern amphibious profile, where the IBPT was shallow and gradually dipped, resistivity values in the top $5\,\mathrm{m}$ remained consistent, regardless of the inundation duration (Fig. 6a). With increasing depth, the sediment at modern or only recently inundated shoreline positions showed a
340 sharp increase in resistivity, rising by several orders of magnitude. In contrast, the shorelines inundated for longer periods exhibited flatter, more stable profiles. Notably, at depths below the deepest point of the IBPT, where the subsurface is frozen, resistivity differences may reflect varying amounts of frozen material within the pore space. We chose $20\,\mathrm{m}$ as our control depth, as it aligned with the DZAA on land and corresponded to a depth where both amphibious profiles were within reliable DOI index on the northern side (Fig.A4). The point furthest from the current shoreline, which had been inundated for nearly 60
345 years, showed no change in resistivity with depth, indicating a stabilized thermal and chemical state. In comparison, the point inundated for 15 years still exhibited a sharp resistivity increase between the surface and $20\,\mathrm{m}$, stabilizing only beyond that depth. For both profiles, the curves representing different inundation periods were naturally sorted from shortest to longest, with the mean resistivity decreasing from highest to lowest as the inundation period increased.

There were differences in the change of bulk sediment resistivity with depth and distance from shoreline between the eastern
350 and western profiles. The resistivity-depth profiles of the western profile reflected the differences in IBPT between the western and eastern profiles. On the western side, the IBPT increases steeply before the 1970 shoreline, reaching a depth of around $20\,\mathrm{m}$. In the top 10 meters below the seabed, the curves are already sorted from higher to lower resistivity.

The analysis of the composition change of the subsurface using inverted resistivities often introduces considerable uncertainty due to the low sensitivity of inverted resistivity models in layered ground with strong resistivity contrasts, common in
355 permafrost conditions (Tomaškovičová and Ingeman-Nielsen, 2025). These effects can be especially pronounced in subsea permafrost environments with conductive seawater overlying unfrozen saline sediment and frozen ground (Arboleda-Zapata et al., 2022). However, the low sensitivity problem can be partially mitigated by deploying electrodes on the seabed instead of using floating electrodes (Sellmann et al., 1989). With respect to our study, the northern offshore sections of the amphibious surveys which crossed the known historical shorelines were less reliable than the terrestrial parts based on the DOI indices
360 (Fig.A4). The reliability of the western profile deeper than $20\,\mathrm{m}$ was also lower than that for the eastern profile.

To make a step towards validation we compared the temporal changes in bulk resistivity (based on place–for–time substitution using historical shoreline positions) to numerical modelling of sediment warming after inundation. Both the inverted and modelled data indicated a decrease in resistivity with increasing inundation time. For the modelled resistivities, the decrease was slight, with a fairly flat trend line, while the inverted resistivities drop of significantly within the 60 years period. On the
365 eastern profile this translates into a decrease from around $1000\,\Omega\,\mathrm{m}$ to $100\,\Omega\,\mathrm{m}$. On the western profile the resistivities drop
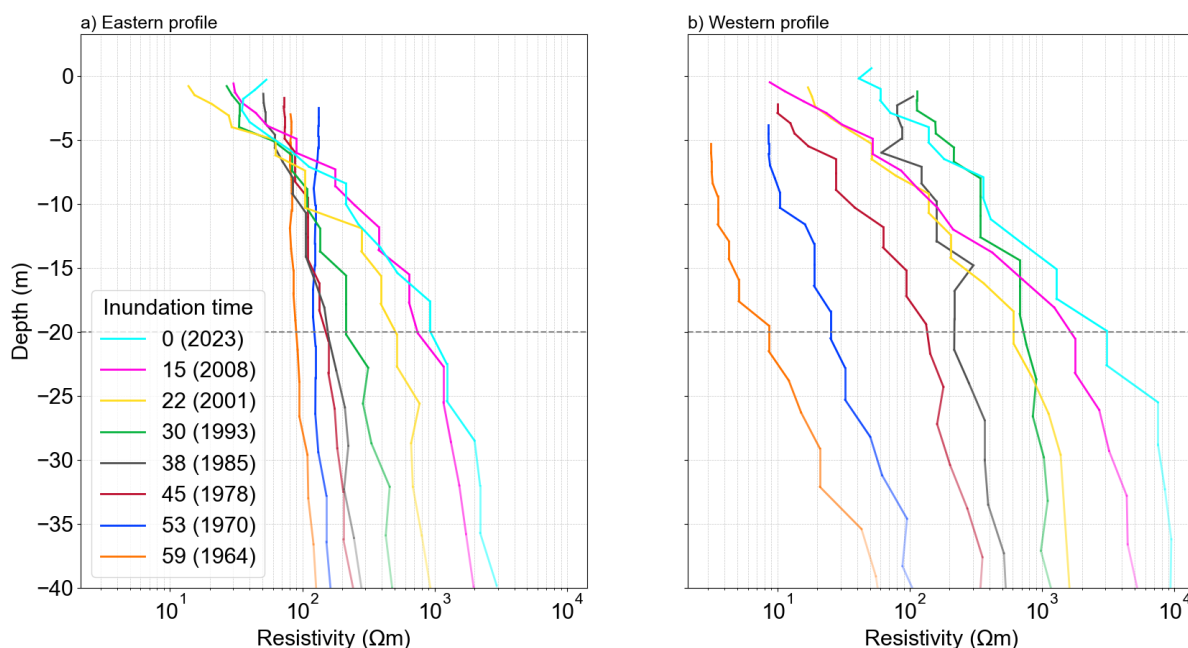
Figure 6. Resistivity-depth profiles for the east and west shorelines over multiple years of inundation. Each line represents a shoreline profile from a different year, with colors corresponding to inundation time. The depth is defined as depth from the seabed. The transparency (alpha) of each segment reflects data coverage, with more opaque lines indicating higher coverage. Dashed horizontal line marks the depth of $20\,\mathrm{m}$ for reference. Resistivity is shown on a logarithmic scale to highlight variations across depths and shoreline locations.

from around $3000\,\Omega\,\mathrm{m}$ to around $10\,\Omega\,\mathrm{m}$. The modelled resistivities at timestep zero align with the inverted resistivities. Modelled temperatures rose sharply from $-5\,°\mathrm{C}$ to above $-3\,°\mathrm{C}$ within the first 18 years, followed by a more gradual increase to above $-1.5\,°\mathrm{C}$ over the subsequent 40 years. Sensitivity analyses revealed a weak influence of the porosity value on the resulting resistivities based on the narrow value range produced by varying the porosity from $\varphi = 0.4$ to $\varphi = 0.6$. The variations

370 in porewater resistivity (R_w) on the other hand yielded a broad range of 2 to 4 orders of magnitude variation in the resulting bulk sediment resistivities. The inverted resistivities mostly fell into this broad range, with an exception of two low values in the late timesteps for the western profile.

4 Discussion

4.1 Permafrost thaw depth

375 Our results indicate the presence of permafrost beneath Tuktoyaktuk Island, supported by both the subsurface resistivity distribution showing elevated values in the terrestrial regions of the survey and the active layer measurements conducted. The
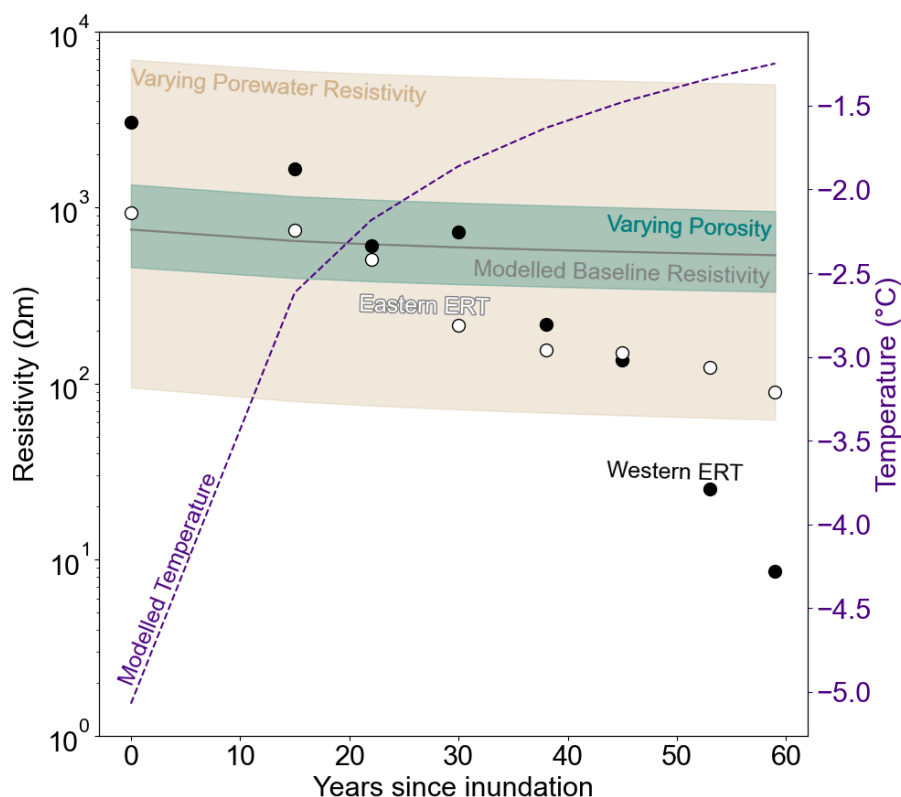
Figure 7. Temperature and modelled and inverted resistivity as a function of time since inundation at 20 m depth. The purple dashed line illustrates the modelled sediment temperatures. The white and black circles represent the inverted resistivities from the eastern and western ERT profiles respectively. The gray line depicts the base case ($\phi = 0.5$, $R_w = 10$ Ωm) modelled bulk sediment resistivity. The teal region represents the range of modelled bulk sediment resistivities corresponding to the porosity range of ($\phi = 0.4 - 0.6$). The tan region represents the range of modelled bulk sediment resistivities corresponding to the porewater resistivity range of $R_w = 1 - 100$ Ωm.

depth to permafrost is relatively shallow, with its deepest ($1.5\,\mathrm{m}$) at the bluff area. These findings align with previous studies reporting high ground ice content and substantial ice masses located at the cliff base (Lapham et al., 2020; Whalen et al., 2022).

The interpolated IBPT offshore shows strong agreement with sediment temperature measurements, shallow water active

380   layer measurements, and borehole observations. Angelopoulos et al. (2024) used passive seismic recordings to determine the IBPT along the lines close to our ERT profiles, reporting on a similar shape of the IBPT north of the island to what we interpolated from ERT, including the sharper dip on the western profile. The calibrated shear wave velocity employed by Angelopoulos et al. (2024) for frequency to depth conversion might not be valid for all the subsurface regions investigated. Therefore, the IBPT depths derived from independent ERT and passive seismic investigations are expected to be different.

385   Along the western profile in the vicinity of the borehole, our estimated IBPT suggests a deeper thaw front compared to the 2018 borehole data. While uncertainties in the ERT data, inversion, or IBPT interpolation could contribute to this discrepancy,

the strong alignment with the borehole data from the eastern profile suggests that some thaw deepening may have occurred between when the borehole was drilled in 2018 and when the resistivity measurements were taken in 2023. The north-south difference of the IBPT, where the northern IBPT is shallower and the southern IBPT is deeper, corroborates findings from Erkens et al. (2025) and illustrates the differences in mean erosion rates between the northern and southern sides of the island, as reported by Hynes et al. (2014). The inclination of the IBPT table depends on coastal retreat rates, with rapid erosion causing a shallower IBPT and slower retreat leading to a steeper inclination due to permafrost degradation (Overduin et al., 2016). For a given distance from the coastline, the mean erosion rate is inversely correlated with marine inundation time. In other words, specific locations offshore of a rapidly eroding coastline have been submerged for shorter periods of time compared to slowly eroding coastlines, leading to less permafrost thaw.

The interpolated IBPT has several uncertainties associated with it. Firstly, this is directly related to the resistivity data and the inversion result. As noted above, the measurement errors were incorporated and the inversion diagnostics showed good fits. The misfit function showed mostly a random noise distribution, with slight clustering of a somewhat lower and higher misfit in certain areas which could lead to minor artefacts (Fig.A3). Secondly, the shape of the curve is highly dependent on the definition and method used. We tested various approaches, including a resistivity cut-off value (Overduin et al., 2012; You et al., 2013; Sherman et al., 2017; Angelopoulos et al., 2019; Pedrazas et al., 2020), the highest gradient in linear space (Erkens et al., 2025), and the highest gradient in logarithmic space (Erkens et al., 2025). Ultimately, we adopted a method that combines elements of all three, guided by a heuristic judgment of whether the interpolated IBPT aligns with observed subsurface trends. One of the main challenges of applying the aforementioned methods was the irregular shape of our inversion mesh, which contrasts with the smoother resistivity contours described in previous studies. Another source of uncertainty comes from the need to smooth out the IBPT. Without smoothing, the interpolation followed the jagged edges of the mesh, so we had to adjust it to create a more realistic representation of the subsurface.

A slight discrepancy between the sediment temperature gradient-derived depth to the IBPT and the interpolated IBPT on the southern side of the eastern profile (red points vs. red dotted line, Fig. 2a) could be explained by the freezing point depression of the soil pore water. As demonstrated by temperature profiles in subsea permafrost measured by Osterkamp and Harrison (1982), the salts can decrease the freezing point by $2\,°C$ to $3\,°C$. Additionally, the absolute depth of the IBPT, particularly northward of borehole 2 on the western profile (north of $250\,m$) may have higher uncertainties since the DOI index was higher (i.e. low reliability) towards the edges of the profiles. Additionally, the three-dimensional structure of the submerged thermokarst basin is unknown, and lateral variations in the IBPT may have influenced the measured voltages.

4.2 Permafrost transition across the shoreface

Osterkamp (2001) identified five potential regions transitioning from terrestrial to subsea conditions, which serve as a useful framework for mapping our results. These regions are summarized as: 1) onshore areas with cold, terrestrial permafrost; 2) the beach zone influenced by waves, high tides, and sea water infiltration; 3) areas where sea ice freezes to the seabed, resulting in cold temperatures and saline brine infiltration; 4) regions where sea ice does not attach to the seabed, and restricted under-ice circulation leads to higher salinities and lower temperatures; and 5) areas with normal sea water over the seabed year-round,

maintaining stable chemical and thermal conditions (Osterkamp, 2001). The terrestrial parts of the amphibious surveys belong to region 1 based on their shallow active layer and high resistivities.

Focusing on the northern parts of the amphibious surveys, the deep active layer on the bluffs and low resistivity areas are representative of the beach zone (region 2: 240–320 m E and 170–220 m W). Whalen et al. (2022) reported a significant
425 sediment loss at the base of the north-east facing cliff resulting from a storm event in 2018. This is consistent with the formation of thermal-erosional niches (Kobayashi, 1985; Jones et al., 2018) and could explain the particularly visible low resistivity zone (below 10 Ωm) close to the northern shoreline of the western amphibious profile. The reduced resistivity could be both attributed to the thermal undercutting, as well as the infiltration of brine which can be pushed up onto the beach during storm floods (Günther et al., 2013). When the beach sediment freezes, salt expulsion can drive brines deeper into the subsurface.

430 We identify the entire remaining northern offshore section of the eastern amphibious survey as well as parts of the western amphibious profile to be representative of region 3 (320 m on E and 220–240 m W), since BFI occurs where the water depth is shallow enough (< 2 m). This is also supported by the evidence from borehole 4, where at the time of drilling in March 2018, the upper $90\,\text{cm}$ were frozen and the water depth at that position was approximately $50\,\text{cm}$. As a result the IBPT in region 3 of our profiles is shallow and dips very slowly as the bathymetry increases. From the subsurface resistivity distribution, we do not
435 observe evidence of sufficient brine infiltration into the seabed to offset freezing from BFI. With an electrode spacing of $5\,\text{m}$, our data may be too coarse to resolve such thin structures.

The region where the IBPT dips very rapidly with deepening of the bathymetric profile provides us with a reference for region 4 within our study region, but only on the western profile. The bathymetric dip in this area is a legacy of the transgressive history of the region, as the steep near-shore slope drops into a submerged thermokarst lake basin (Forbes et al., 2014). Borehole
440 2 data suggests that sea ice does not extend to the seabed at that location, consistent with the water depth of more than $3\,\text{m}$. Osterkamp (2001) states that freezing of the sediment does not necessarily require direct contact with the sea ice because brine drainage from growing sea ice raises water salinity and lowers seabed water temperature to maintain phase equilibrium. We do not see this signal of a cooling seabed in region 4 from the subsurface resistivity distributions and the interpolated IBPT. This may be due to the distance between the seabed and the bottom of the sea ice: based on the Borehole 2 data this is more than $2\,\text{m}$
445 which could give the brine more circulation and dispersion space. Additionally, the combination of an increased open water season and positive annual mean temperature maintained in the bay (Fig. 5c), result in sediment potentially warming through seawater. The steep lowering of the IBPT to a depth beyond $30\,\text{m}$ in the areas where the water depth does not exceed $3.5\,\text{m}$ attests to the warming signal dominating over the brine expulsion-induced seabed cooling, or to the influence of thawing prior to marine inundation, for example in a thermokarst basin.

450 The differences in IBPT inclination in the northern offshore regions of the eastern and western amphibious surveys are unlikely to reflect variations in inundation rates, given the profiles' proximity and the consistent historical shorelines along the island's northeast-facing cliff. Instead, the steep IBPT in the northern section of the western profile may indicate enhanced thawing beneath the submerged thermokarst lake basin due to the deepening bathymetry and/or prior to inundation.

4.3 Long-term effects of inundation on the subsurface composition

455 On the island, seasonal air temperature variations have minimal influence at 20 m depth below the surface. We assume the same for temperature variations in subsea permafrost since seabed temperatures, which are separated from air temperature variations by overlying sea water and sea ice and usually vary less than ground surface air temperatures. Air temperatures from the Tuktoyaktuk airport meteorological station for the 1–year period of 22.03.2023 to 21.03.2024 showed FDD and Thawing degree days TDD of 4378 and 1370 degrees–days, respectively. Annual FDD/TDD values measured at bottom moorings in 4

460 and 7 m water depths (Sep. 2023–Aug. 2024) were 73/989 and 252/620 degree–days, respectively. As a result, smaller seabed temperature fluctuations drive even smaller amplitude temperature changes at depth. Thus, resistivity is expected to change slowly over time at depth and to reflect long-term inundation effects on the thermal state of subsea permafrost (Fig. 7).

The temporal trend in inverted bulk sediment resistivities shows a decrease of up to 3 orders of magnitude within 60 years of inundation. During the first 15 years, resistivities on the western profile were consistently higher than those on the eastern

465 profile, converging around 20 years post-inundation and remaining similar until approximately year 45. An exception occurs at around year 30, when the western profile again exhibits a pronounced increase in resistivity. This may reflect cooling related to BFI formation, a pattern that appears more prominently in the western profile than in the eastern.

Inverted resistivity values are always subject to uncertainty, particularly in settings with high subsurface heterogeneity. In such cases, inversion results tend to amplify contrasts, leading to more pronounced highs and lows compared to what might be

470 expected in a smoother, more homogeneous model. This effect is especially evident in the western profile, where the presence of a submerged thermokarst lake basin and a deep IBPT dip introduces greater data amplitude. As a result, the inversion would show higher resistivity beneath the island on the western side compared to the eastern profile, even though the actual subsurface conditions may be similar—unless, for instance, a massive ice body is present along the western line.

Our IBPT interpolation indicates that the transition from unfrozen to frozen sediments typically occurs within the $10\,\Omega\,\mathrm{m}$ to

475 $100\,\Omega\,\mathrm{m}$ resistivity range. The inverted resistivities of the eastern profile remain above this threshold throughout the simulation, suggesting that the sediments remain largely frozen. In contrast, the final two time steps of the western profile fall below this range, indicating unfrozen conditions. These time steps coincide with shoreline positions where the western profile intersects a thermokarst lake basin and a deep IBPT depression. As such, we interpret these changes in resistivity as local effects rather than representative of broader erosion-driven trends. However, even in the eastern profile—where the IBPT remains relatively stable

480 without sharp dips—substantial changes in resistivity at depth are observed. Within 60 years of inundation, values approach the critical $100\,\Omega\,\mathrm{m}$ threshold, suggesting significant thawing is occurring even under conditions where the IBPT geometry is more gradual.

The modelled resistivity time series demonstrated a decreasing trend in resistivity with inundation. We made a liberal assumption for the model setup, assuming instantaneous inundation with a shift from a ground surface exposed to lower $(-8.2\,^\circ\mathrm{C})$

485 mean annual air temperatures to a seabed exposed to higher $(2.2\,^\circ\mathrm{C})$ mean annual water temperatures within just one time step. This is equivalent to an immediate transition from region 1 to 5 based on classification given by Osterkamp (2001). In reality, there would be a prolonged transition period between these two states through the intermediate regions, whereby the sediment

would erode only gradually, resulting in only a shallow water layer above and allowing for BFI formation and subsequent cooling, which could act to delay permafrost thaw. Even under this extreme warming scenario, our modelled resistivities exhibit a relatively flat, slightly decreasing trend, whereas the inverted resistivities show a decline spanning multiple orders of magnitude.

Since both the modelled and inverted resistivities align at the initial time step, we conclude that the thermal model successfully reproduced the starting conditions. However, the discrepancy in the rate of resistivity change between the model and the inversion suggests that subsurface composition changes are influenced by more than just thermal forcing. Other factors could be the infiltration of saline seawater into the sediments or lateral heat transport. Measurements from both the mooring station and CTD profiles indicate that the surrounding seawater is relatively saline, with resistivities ranging between $1\,\Omega\,\mathrm{m}$ to $4\,\Omega\,\mathrm{m}$. Even then, for such infiltration to significantly affect resistivity values down to depths of $20\,\mathrm{m}$ below the seabed, the process would need to be particularly intense. While salt diffusion is very slow, brine density-driven flow through coarse sediments is relatively rapid (Harrison and Osterkamp, 1978). Given the silt-dominated texture of the sediments, we suspect additional mechanisms beyond saltwater infiltration are likely contributing to the rapid decrease in bulk resistivity. Perhaps a relatively higher proportions of clays are present in the thermokarst basin, leading to lower resistivity values (Solomon et al., 2000).

This raises the question of whether the heat from adjacent unfrozen sediments could laterally propagate toward the island, potentially contributing to the formation or persistence of thermal niches. Evidence supporting this possibility includes the lower resistivity values at depth observed for the oldest shoreline positions along the western profile, as well as the more rapid rate of resistivity decline over time, ultimately leading to $R_{western} < R_{eastern}$ for the final two shoreline positions. This pattern suggests that warming is not solely driven by vertical heat conduction from the seabed but may also involve lateral heat transfer from already thawed or thawing regions, such as the thermokarst basin to the west. If so, the effects of pre-inundation thaw, including those associated with thermokarst lake formation, could persist and influence the thermal regime for decades after inundation (e.g. Malakhova, 2016). This interpretation is consistent with findings by Angelopoulos et al. (2021), who documented sustained thawing due to legacy thermal conditions in similar Arctic coastal environments.

5 Conclusions

We investigated permafrost beneath and around Tuktoyaktuk Island, NWT, Canada, using amphibious ERT in combination with historical shoreline data to examine the effects of coastal erosion on permafrost evolution. Our results show that permafrost beneath the island is undergoing significant transitions along the northern shoreline where terrestrial permafrost is actively converting to subsea permafrost due to ongoing coastal retreat. Up to six decades of inundation have led to a notable deepening of the permafrost table, with inverted resistivity data revealing a consistent long-term decrease in bulk sediment resistivity below the inferred boundary between unfrozen and frozen ground. This trend reflects a general warming of the subsurface following inundation. However, thermal modelling indicates that conductive heat transfer alone is insufficient to explain the magnitude and rate of the observed resistivity changes. This discrepancy points to additional contributing processes. Infiltration of saline seawater into the sediment column likely plays a role, as well as the submergence of previously thawed sediments

(taliks) beneath lakes. Furthermore, the evidence of potential lateral heat transfer from taliks suggests that the legacy of pre-inundation thermal conditions can persist for decades after submergence. As the coastlines continue to erode in response to warming temperatures, increased wave action, and diminishing sea ice cover, processes that accelerate subsea permafrost thaw will likely contribute to the structural destabilization of Tuktoyaktuk Island if remained unprotected. Understanding these

525   dynamics is critical for anticipating landscape change and associated geohazards in rapidly warming polar regions.

Data availability. Sources of data used in this study are cited or else the data are available from the PANGAEA Data Publisher for Earth and Environmental Science as follows:

CTD data: https://doi.pangaea.de/10.1594/PANGAEA.982777.

Van Veen grab samples: https://doi.pangaea.de/10.1594/PANGAEA.981226.

530   Marine GPS and echo-sounder: https://doi.pangaea.de/10.1594/PANGAEA.981227.

ERT: https://doi.pangaea.de/10.1594/PANGAEA.981228.

References

Angelopoulos, M., Westermann, S., Overduin, P., Faguet, A., Olenchenko, V., Grosse, G., and Grigoriev, M. N.: Heat and Salt Flow in Subsea Permafrost Modeled with CryoGRID2, Journal of Geophysical Research: Earth Surface, 124, 920–937, https://doi.org/10.1029/2018JF004823, 2019.

Angelopoulos, M., Overduin, P. P., Miesner, F., Grigoriev, M. N., and Vasiliev, A. A.: Recent advances in the study of Arctic submarine permafrost, Permafrost and Periglacial Processes, 31, 442–453, https://doi.org/10.1002/ppp.2061, 2020.

Angelopoulos, M., Overduin, P. P., Jenrich, M., Nitze, I., Günther, F., Strauss, J., Westermann, S., Schirrmeister, L., Kholodov, A., Krautblatter, M., Grigoriev, M. N., and Grosse, G.: Onshore Thermokarst Primes Subsea Permafrost Degradation, Geophysical Research Letters, 48, e2021GL093 881, https://doi.org/10.1029/2021GL093881, 2021.

Angelopoulos, M., Ryberg, T., Rasmussen, C. F., Haberland, C., Juhls, B., Dallimore, S., Boike, J., and Overduin, P. P.: Passive Seismology: Lightweight and Rapid Detection of Arctic Subsea and Sub-Aquatic Permafrost, Journal of Geophysical Research: Earth Surface, 129, e2023JF007 290, https://doi.org/10.1029/2023JF007290, 2024.

Angelopoulos, M., Aliyeva, M., Cable, W. L., and Overduin, P. P.: CTD measurements acquired in the region of Inuvik, Tuktoyaktuk and the Mackenzie Delta, Northwest Territories, Canada, https://doi.org/https://doi.pangaea.de/10.1594/PANGAEA.982777, 2025a.

Angelopoulos, M., Aliyeva, M., Cable, W. L., and Overduin, P. P.: Van Veen grab samples acquired in the region of Inuvik, Tuktoyaktuk and the Mackenzie Delta, Northwest Territories, Canada, https://doi.pangaea.de/10.1594/PANGAEA.981226, 2025b.

Arboleda-Zapata, M., Angelopoulos, M., Overduin, P. P., Grosse, G., Jones, B. M., and Tronicke, J.: Exploring the capabilities of electrical resistivity tomography to study subsea permafrost, The Cryosphere, 16, 4423–4445, https://doi.org/10.5194/tc-16-4423-2022, 2022.

Archie, G.: The Electrical Resistivity Log as an Aid in Determining Some Reservoir Characteristics, Transactions of the AIME, 146, 54–62, https://doi.org/10.2118/942054-G, 1942.

Arenson, L. U., Brooks, H., Scott, F., Duckett, F., and Klengenberg, C.: Design and Construction of a Coastal Erosion Mitigation Project in Tuktoyaktuk, Northwest Territories, in: 78th Canadian Geotechnical Conference, Winnipeg, MN, 2025.

Arvai, K.: kneed, https://doi.org/10.5281/zenodo.6496267, 2020.

Aré, F. E.: Thermal abrasion of sea coasts (part I), Polar Geography and Geology, 12, 1–1, https://doi.org/10.1080/10889378809377343, 1988.

Aré, F. E.: Shoreface of the Arctic seas - a natural laboratory for subsea permafrost dynamics, in: Proceedings of the Eigth International Conference on Permafrost, edited by Phillips, M., Springman, S. M., and Arenson, L. U., vol. 1, pp. 27–32, Balkema, Lisse, The Netherlands, ISBN 978-90-5809-584-8, 2003.

Bateman, M. D. and Murton, J. B.: The chronostratigraphy of Late Pleistocene glacial and periglacial aeolian activity in the Tuktoyaktuk Coastlands, NWT, Canada, Quaternary Science Reviews, 25, 2552–2568, https://doi.org/10.1016/j.quascirev.2005.07.023, 2006.

Biskaborn, B. K., Smith, S. L., Noetzli, J., Matthes, H., Vieira, G., Streletskiy, D. A., Schoeneich, P., Romanovsky, V. E., Lewkowicz, A. G., Abramov, A., Allard, M., Boike, J., Cable, W. L., Christiansen, H. H., Delaloye, R., Diekmann, B., Drozdov, D., Etzelmüller, B., Grosse, G., Guglielmin, M., Ingeman-Nielsen, T., Isaksen, K., Ishikawa, M., Johansson, M., Johannsson, H., Joo, A., Kaverin, D., Kholodov, A., Konstantinov, P., Kröger, T., Lambiel, C., Lanckman, J.-P., Luo, D., Malkova, G., Meiklejohn, I., Moskalenko, N., Oliva, M., Phillips, M., Ramos, M., Sannel, A. B. K., Sergeev, D., Seybold, C., Skryabin, P., Vasiliev, A., Wu, Q., Yoshikawa, K., Zheleznyak, M., and Lantuit, H.: Permafrost is warming at a global scale, Nat Commun, 10, 264, https://doi.org/10.1038/s41467-018-08240-4, publisher: Nature Publishing Group, 2019.

570   Boike, J. and Dallimore, S. R.: Summary of 2018 Mackenzie Delta permafrost field campaign (mCAN2018), Northwest Territories, Tech. Rep. 8640, Natural Resources Canada, https://doi.org/10.4095/315704, 2019.

Bostock, H. S.: Physiographic regions of Canada, https://ostrnrcan-dostrncan.canada.ca/handle/1845/112154, 1970.

Burn, C. R.: Permafrost, land and water, Natural history of the Western Arctic. Inuvik, Northwest Territories: Western Arctic Handbook Committee, pp. 19–23, 2002.

575   Coscia, I., Greenhalgh, S. A., Linde, N., Doetsch, J., Marescot, L., Günther, T., Vogt, T., and Green, A. G.: 3D crosshole ERT for aquifer characterization and monitoring of infiltrating river water, GEOPHYSICS, 76, G49–G59, https://doi.org/10.1190/1.3553003, 2011.

Couture, R., Robinson, S., Burgess, M. M., and Solomon, S. M.: Climate change, permafrost, and community infrastructure: a compilation of background material from a pilot study of Tuktoyaktuk, Northwest Territories, Tech. Rep. 3867, Natural Resources Canada, https://doi.org/10.4095/213753, 2002.

580   Creel, R., Guimond, J., Jones, B. M., Nielsen, D. M., Bristol, E., Tweedie, C. E., and Overduin, P. P.: Permafrost thaw subsidence, sea-level rise, and erosion are transforming Alaska's Arctic coastal zone, Proceedings of the National Academy of Sciences, 121, e2409411121, https://doi.org/10.1073/pnas.2409411121, publisher: Proceedings of the National Academy of Sciences, 2024.

Dall'Amico, M., Endrizzi, S., Gruber, S., and Rigon, R.: A robust and energy-conserving model of freezing variably-saturated soil, The Cryosphere, 5, 469–484, https://doi.org/10.5194/tc-5-469-2011, 2011.

585   Dallimore, S. R., Wolfe, S. A., and Solomon, S. M.: Influence of ground ice and permafrost on coastal evolution, Richards Island, Beaufort Sea coast, N.W.T., Can. J. Earth Sci., 33, 664–675, https://doi.org/10.1139/e96-050, 1996.

Environment and Climate Change Canada: Climate Data Extraction Tool, https://climate-change.canada.ca/climate-data/#/daily-climate-data, last Modified: 2025-02-03T16:21:16.098Z, 2025.

Erkens, E., Angelopoulos, M., Tronicke, J., Dallimore, S. R., Whalen, D., Boike, J., and Overduin, P. P.: Mapping subsea permafrost
590   around Tuktoyaktuk Island (Northwest Territories, Canada) using electrical resistivity tomography, The Cryosphere, 19, 997–1012, https://doi.org/10.5194/tc-19-997-2025, 2025.

Forbes, D. L., Manson, G. K., Whalen, D. J. R., Couture, N. J., and Hill, P. R.: Coastal products of marine transgression in cold-temperate and high-latitude coastal-plain settings: Gulf of St Lawrence and Beaufort Sea, The Geological Society of London, Special Publications, 388, 131–163, https://doi.org/10.1144/SP388.18, 2014.

595   Fortier, R., Allard, M., and Seguin, M. K.: Effect of physical properties of frozen ground on electrical resistivity logging, Cold Regions Science and Technology, 22, 361–384, https://doi.org/10.1016/0165-232X(94)90021-3, 1994.

Glover, P. W. J.: A generalized Archie's law for n phases, Geophysics, 75, E247–E265, https://doi.org/10.1190/1.3509781, 2010.

Groenke, B.: CryoGrid/FreezeCurves.jl: v0.9.3, https://doi.org/10.5281/zenodo.15269555, 2025.

Groenke, B. and Nitzbon, J.: CryoGrid/CryoGrid.jl: v0.23.1, https://doi.org/10.5281/zenodo.14562199, 2024.

600   Groenke, B., Langer, M., Nitzbon, J., Westermann, S., Gallego, G., and Boike, J.: Investigating the thermal state of permafrost with Bayesian inverse modeling of heat transfer, The Cryosphere, 17, 3505–3533, https://doi.org/10.5194/tc-17-3505-2023, 2023.

Günther, F., Overduin, P. P., Makarov, A., and Grigoriev, M. N.: Russian-German cooperation SYSTEM LAPTEV SEA : the Expeditions Laptev Sea - Mamontov Klyk 2011 & Buor Khaya 2012, Tech. rep., Alfred Wegener Institute for Polar and Marine Research, Bremerhaven, Germany, DOI:10.2312/BzPM_0664_2013, 2013.

605   Günther, T. and Rücker, C.: Boundless Electrical Resistivity Tomography BERT 2 – the user tutorial, 2018.

Günther, T., Rücker, C., and Spitzer, K.: Three-dimensional modelling and inversion of dc resistivity data incorporating topography — II. Inversion, Geophysical Journal International, 166, 506–517, https://doi.org/10.1111/j.1365-246X.2006.03011.x, 2006.

Hansen, P. C. and O'Leary, D. P.: The Use of the L-Curve in the Regularization of Discrete Ill-Posed Problems, SIAM J. Sci. Comput., 14, 1487–1503, https://doi.org/10.1137/0914086, publisher: Society for Industrial and Applied Mathematics, 1993.

Harper, J. R.: Morphology of the Canadian Beaufort Sea coast, Marine Geology, 91, 75–91, https://doi.org/10.1016/0025-3227(90)90134-6, 1990.

Harrison, W. D. and Osterkamp, T. E.: Heat and mass transport processes in subsea permafrost 1. An analysis of molecular diffusion and its consequences, Journal of Geophysical Research: Oceans, 83, 4707–4712, https://doi.org/10.1029/JC083iC09p04707, 1978.

Hauck, C.: Frozen ground monitoring using DC resistivity tomography, Geophysical Research Letters, 29, 12–1–12–4, https://doi.org/10.1029/2002GL014995, 2002.

Herring, T., Lewkowicz, A. G., Hauck, C., Hilbich, C., Mollaret, C., Oldenborger, G. A., Uhlemann, S., Farzamian, M., Calmels, F., and Scandroglio, R.: Best practices for using electrical resistivity tomography to investigate permafrost, Permafrost and Periglacial Processes, 34, 494–512, https://doi.org/10.1002/ppp.2207, 2023.

Hilbich, C., Marescot, L., Hauck, C., Loke, M. H., and Mäusbacher, R.: Applicability of electrical resistivity tomography monitoring to coarse blocky and ice-rich permafrost landforms, Permafrost and Periglacial Processes, 20, 269–284, https://doi.org/10.1002/ppp.652, 2009.

Hill, P. R., Mudie, P. J., Moran, K., and Blasco, S. M.: A sea-level curve for the Canadian Beaufort Shelf, Can. J. Earth Sci., 22, 1383–1393, https://doi.org/10.1139/e85-146, 1985.

Hu, K., Issler, D. R., Chen, Z., and Brent, T. A.: Permafrost investigation by well logs, and seismic velocity and repeated shallow temperature surveys, Beaufort-Mackenzie Basin, Tech. Rep. 6956, Natural Resources Canada, https://doi.org/10.4095/293120, 2013.

Hynes, S., Solomon, S. M., and Whalen, D.: GIS compilation of coastline variability spanning 60 years in the Mackenzie Delta and Tuktoyaktuk in the Beaufort Sea, Tech. Rep. 7685, Natural Resources Canada, https://doi.org/10.4095/295579, 2014.

IOC, SCOR, and IAPSO: The International Thermodynamic Equation of Seawater – 2010: Calculation and Use of Thermodynamic Properties, issue: 203 Pages: 196 Publication Title: Intergovernmental Oceanographic Commission, UNESCO Manuals and Guides No. 56, 2010.

Johnson, K., Solomon, S., Berry, D., and Graham, P.: Erosion progression and adaptation strategy in a northern coastal community, in: 8th international conference on Permafrost, pp. 21–25, 2003.

Jones, B. M., Farquharson, L. M., Baughman, C. A., Buzard, R. M., Arp, C. D., Grosse, G., Bull, D. L., Günther, F., Nitze, I., Urban, F., Kasper, J. L., Frederick, J. M., Thomas, M., Jones, C., Mota, A., Dallimore, S., Tweedie, C., Maio, C., Mann, D. H., Richmond, B., Gibbs, A., Xiao, M., Sachs, T., Iwahana, G., Kanevskiy, M., and Romanovsky, V. E.: A decade of remotely sensed observations highlight complex processes linked to coastal permafrost bluff erosion in the Arctic, Environ. Res. Lett., 13, 115 001, https://doi.org/10.1088/1748-9326/aae471, 2018.

Jones, B. M., Arp, C. D., Grosse, G., Nitze, I., Lara, M. J., Whitman, M. S., Farquharson, L. M., Kanevskiy, M., Parsekian, A. D., Breen, A. L., Ohara, N., Rangel, R. C., and Hinkel, K. M.: Identifying historical and future potential lake drainage events on the western Arctic coastal plain of Alaska, Permafrost and Periglacial Processes, 31, 110–127, https://doi.org/10.1002/ppp.2038, 2020.

Kneisel, C., Hauck, C., Fortier, R., and Moorman, B.: Advances in geophysical methods for permafrost investigations, Permafrost and Periglacial Processes, 19, 157–178, https://doi.org/10.1002/ppp.616, 2008.

Kobayashi, N.: Formation of thermoerosional niches into frozen bluffs due to storm surges on the Beaufort Sea coast, Journal of Geophysical Research: Oceans, 90, 11 983–11 988, https://doi.org/10.1029/JC090iC06p11983, 1985.

645 Kokelj, S. V., Palmer, M. J., Lantz, T. C., and Burn, C. R.: Ground Temperatures and Permafrost Warming from Forest to Tundra, Tuktoyaktuk Coastlands and Anderson Plain, NWT, Canada, Permafrost and Periglacial Processes, 28, 543–551, https://doi.org/10.1002/ppp.1934, 2017.

Lantuit, H., Overduin, P. P., and Wetterich, S.: Recent Progress Regarding Permafrost Coasts, Permafrost and Periglacial Processes, 24, 120–130, https://doi.org/10.1002/ppp.1777, 2013.

650 Lapham, L. L., Dallimore, S. R., Magen, C., Henderson, L. C., Powers, L. C., Gonsior, M., Clark, B., Côté, M., Fraser, P., and Orcutt, B. N.: Microbial Greenhouse Gas Dynamics Associated With Warming Coastal Permafrost, Western Canadian Arctic, Front. Earth Sci., 8, https://doi.org/10.3389/feart.2020.582103, 2020.

Loke, M. H. and Lane, J. W., J.: Inversion of Data from Electrical Resistivity Imaging Surveys in Water-Covered Areas, Exploration Geophysics, 35, 266–271, https://doi.org/10.1071/EG04266, 2004.

655 MacLeod, R. F. and Dallimore, S. R.: Assessment of Storm Surge History as Recorded by Driftwood in the Mackenzie Delta and Tuktoyaktuk Coastlands, Arctic Canada, Front. Earth Sci., 9, https://doi.org/10.3389/feart.2021.698660, 2021.

Malakhova, V. V.: On the thermal influence of thermokarst lakes on the subsea permafrost evolution, in: 22nd International Symposium on Atmospheric and Ocean Optics: Atmospheric Physics, vol. 10035, pp. 1246–1254, SPIE, https://doi.org/10.1117/12.2248714, 2016.

Miesner, F., Cable, W. L., and Boike, J.: Temperature measurements at three subaquatic sites in the Mackenzie Delta, Northwest Territories, 660 Canada, https://doi.org/10.1594/PANGAEA.949290, 2022.

Miesner, F., Cable, W. L., Overduin, P. P., and Boike, J.: Brief communication: Testing a portable Bullard-type temperature lance confirms highly spatially heterogeneous sediment temperatures under shallow bodies of water in the Arctic, The Cryosphere, 18, 2603–2611, https://doi.org/10.5194/tc-18-2603-2024, 2024.

Murton, J. B., Waller, R. I., Hart, J. K., Whiteman, C. A., Pollard, W. H., and Clark, I. D.: Stratigraphy and glaciotectonic structures of 665 permafrost deformed beneath the northwest margin of the Laurentide ice sheet, Tuktoyaktuk Coastlands, Canada, Journal of Glaciology, 50, 399–412, https://doi.org/10.3189/172756504781829927, 2004.

Murton, J. B., Frechen, M., and Maddy, D.: Luminescence dating of mid- to Late Wisconsinan aeolian sand as a constraint on the last advance of the Laurentide Ice Sheet across the Tuktoyaktuk Coastlands, western Arctic Canada, Can. J. Earth Sci., 44, 857–869, https://doi.org/10.1139/e07-015, 2007.

670 Oldenburg, D. W. and Li, Y.: Estimating depth of investigation in DC resistivity and IP surveys, Geophysics, 64, 403–416, https://doi.org/10.1190/1.1444545, 1999.

Oldenburg, D. W. and Li, Y.: 5. Inversion for Applied Geophysics: A Tutorial, in: Near-Surface Geophysics, Investigations in Geophysics, pp. 89–150, Society of Exploration Geophysicists, ISBN 978-1-56080-130-6, https://doi.org/10.1190/1.9781560801719.ch5, 2005.

Osterkamp, T. E.: Sub-sea Permafrost, in: Encyclopedia of Ocean Sciences, edited by Steele, J. H., pp. 2902–2912, Academic Press, Oxford, 675 ISBN 978-0-12-227430-5, https://doi.org/10.1006/rwos.2001.0008, 2001.

Osterkamp, T. E. and Harrison, W. D.: Temperature measurements in subsea permafrost off the coast of Alaska, in: 4th Canadian Permafrost Conference, pp. 238–248, Citeseer, https://citeseerx.ist.psu.edu/document?repid=rep1&type=pdf&doi= 1d4eea00bc65cdbd268b0b49a507819edb8369ef, 1982.

Ouellette, D. S.: Thermal and Mechanical Modeling of Coastal Erosion Processes on Tuktoyaktuk Island, Northwest Territories, Master's 680 thesis, University of Calgary, Calgary, Canada, http://hdl.handle.net/1880/113949, 2021.

Overduin, P. P., Westermann, S., Yoshikawa, K., Haberlau, T., Romanovsky, V., and Wetterich, S.: Geoelectric observations of the degradation of nearshore submarine permafrost at Barrow (Alaskan Beaufort Sea), Journal of Geophysical Research: Earth Surface, 117, https://doi.org/10.1029/2011JF002088, 2012.

Overduin, P. P., Wetterich, S., Günther, F., Grigoriev, M. N., Grosse, G., Schirrmeister, L., Hubberten, H.-W., and Makarov, A.: Coastal dynamics and submarine permafrost in shallow water of the central Laptev Sea, East Siberia, The Cryosphere, 10, 1449–1462, https://doi.org/10.5194/tc-10-1449-2016, 2016.

Pedrazas, M. N., Cardenas, M. B., Demir, C., Watson, J. A., Connolly, C. T., and McClelland, J. W.: Absence of ice-bonded permafrost beneath an Arctic lagoon revealed by electrical geophysics, Science Advances, 6, eabb5083, https://doi.org/10.1126/sciadv.abb5083, 2020.

Ramage, J., Jungsberg, L., Wang, S., Westermann, S., Lantuit, H., and Heleniak, T.: Population living on permafrost in the Arctic, Popul Environ, 43, 22–38, https://doi.org/10.1007/s11111-020-00370-6, 2021.

Rampton, V. N.: Quaternary geology of the Tuktoyaktuk Coastlands, Northwest Territories, Energy, Mines and Resources Canada, Canada, ISBN 0-660-12743-1, 1988.

Rampton, V. N. and Bouchard, M.: Surficial Geology of Tuktoyaktuk area, District of Mackenzie, https://doi.org/10.4095/109032, 1975.

Ryberg, T., Cable, W., Overduin, P., and Haberland, C.: Ambient seismic noise data from the shallow sea floor off Tuktoyaktuk, Canada, https://doi.org/10.5880/GIPP.201899.1, 2020.

Ryberg, T., Haberland, C., Overduin, P., and Cable, W.: Subaquatic ambient seismic noise recordings acquired in the region of Inuvik and Tuktoyaktuk, Northwest Territories, Canada, https://doi.org/10.5880/GIPP.202199.1, 2022.

Rücker, C., Günther, T., and Wagner, F. M.: pyGIMLi: An open-source library for modelling and inversion in geophysics, Computers & Geosciences, 109, 106–123, https://doi.org/10.1016/j.cageo.2017.07.011, 2017.

Satopaa, V., Albrecht, J., Irwin, D., and Raghavan, B.: Finding a "Kneedle" in a Haystack: Detecting Knee Points in System Behavior, in: 2011 31st International Conference on Distributed Computing Systems Workshops, pp. 166–171, https://doi.org/10.1109/ICDCSW.2011.20, 2011.

Scott, F., Duckett, F., Arenson, L., Klengenberg, C., and Elias, E.: Erosion Mitigation Design in the Arctic Considering Climate Change Impacts, Coastal Engineering Proceedings, pp. 25–25, https://doi.org/10.9753/icce.v37.structures.25, number: 37, 2022.

Sellmann, P. V., Delaney, A. J., and Arcone, S. A.: Coastal Subsea Permafrost and Bedrock Observations Using DC Resistivity, Final 89-13, U.S. Army Cold Regions Research and Engineering Laboratory, https://apps.dtic.mil/sti/citations/ADA210784, 1989.

Shakhova, N., Semiletov, I., Gustafsson, O., Sergienko, V., Lobkovsky, L., Dudarev, O., Tumskoy, V., Grigoriev, M., Mazurov, A., Salyuk, A., Ananiev, R., Koshurnikov, A., Kosmach, D., Charkin, A., Dmitrevsky, N., Karnaukh, V., Gunar, A., Meluzov, A., and Chernykh, D.: Current rates and mechanisms of subsea permafrost degradation in the East Siberian Arctic Shelf, Nat Commun, 8, 15 872, https://doi.org/10.1038/ncomms15872, 2017.

Sherman, D., Kannberg, P., and Constable, S.: Surface towed electromagnetic system for mapping of subsea Arctic permafrost, Earth and Planetary Science Letters, 460, 97–104, https://doi.org/10.1016/j.epsl.2016.12.002, 2017.

Solomon, S., Mudie, P. J., Cranston, R., Hamilton, T., Thibaudeau, S. A., and Collins, E. S.: Characterisation of marine and lacustrine sediments in a drowned thermokarst embayment, Richards Island, Beaufort Sea, Canada, Int J Earth Sci, 89, 503–521, https://doi.org/10.1007/s005310000126, 2000.

Solomon, S. M.: Spatial and temporal variability of shoreline change in the Beaufort-Mackenzie region, northwest territories, Canada, Geo-Mar Lett, 25, 127–137, https://doi.org/10.1007/s00367-004-0194-x, 2005.

Statistics Canada: Census profile, 2021 census of population, https://www12.statcan.gc.ca/census-recensement/2021/dp-pd/prof/index.cfm?Lang=E, 2022.

720 The Hamlet of Tuktoyaktuk: The Hamlet of Tuktoyaktuk Website, https://tuktoyaktuk.ca/, 2024.

Tiab, D. and Donaldson, E.: Petrophysics: Theory and Practice of Measuring Reservoir Rock and Fluid Transport Properties: Second Edition, Gulf Professional Publishing, 3rd edn., ISBN 978-0-12-383848-3, 2003.

Tikhonov, A. N.: On the solution of incorrectly stated problems and a method of regularization, in: Dokl. Acad. Nauk. SSSR, vol. 151, pp. 501–504, https://cir.nii.ac.jp/crid/1573105975604348544, 1963.

725 Timmermans, M.-L. and Labe, Z. M.: NOAA Arctic Report Card 2024 : Sea Surface Temperature, Technical Report, NOAA, https://doi.org/10.25923/9z96-aq19, 2024.

Tomaškovičová, S. and Ingeman-Nielsen, T.: Validation of four resistivity mixing models on field time lapse geoelectrical measurements from fine-grained soil undergoing freeze-thaw cycles, Journal of Applied Geophysics, 232, 105 572, https://doi.org/10.1016/j.jappgeo.2024.105572, 2025.

730 Westermann, S., Ingeman-Nielsen, T., Scheer, J., Aalstad, K., Aga, J., Chaudhary, N., Etzelmüller, B., Filhol, S., Kääb, A., Renette, C., Schmidt, L. S., Schuler, T. V., Zweigel, R. B., Martin, L., Morard, S., Ben-Asher, M., Angelopoulos, M., Boike, J., Groenke, B., Miesner, F., Nitzbon, J., Overduin, P., Stuenzi, S. M., and Langer, M.: The CryoGrid community model (version 1.0) – a multi-physics toolbox for climate-driven simulations in the terrestrial cryosphere, Geoscientific Model Development, 16, 2607–2647, https://doi.org/10.5194/gmd-16-2607-2023, 2023.

735 Whalen, D., Forbes, D., Kostylev, V., Lim, M., Fraser, P., Nedimović, M., and Stuckey, S.: Mechanisms, volumetric assessment, and prognosis for rapid coastal erosion of Tuktoyaktuk Island, an important natural barrier for the harbour and community, Can. J. Earth Sci., 59, 945–960, https://doi.org/10.1139/cjes-2021-0101, 2022.

Yoshikawa, K., Leuschen, C., Ikeda, A., Harada, K., Gogineni, P., Hoekstra, P., Hinzman, L., Sawada, Y., and Matsuoka, N.: Comparison of geophysical investigations for detection of massive ground ice (pingo ice), Journal of Geophysical Research: Planets, 111, 740 https://doi.org/10.1029/2005JE002573, 2006.

You, Y., Yu, Q., Pan, X., Wang, X., and Guo, L.: Application of electrical resistivity tomography in investigating depth of permafrost base and permafrost structure in Tibetan Plateau, Cold Regions Science and Technology, 87, 19–26, https://doi.org/10.1016/j.coldregions.2012.11.004, 2013.

Appendix A
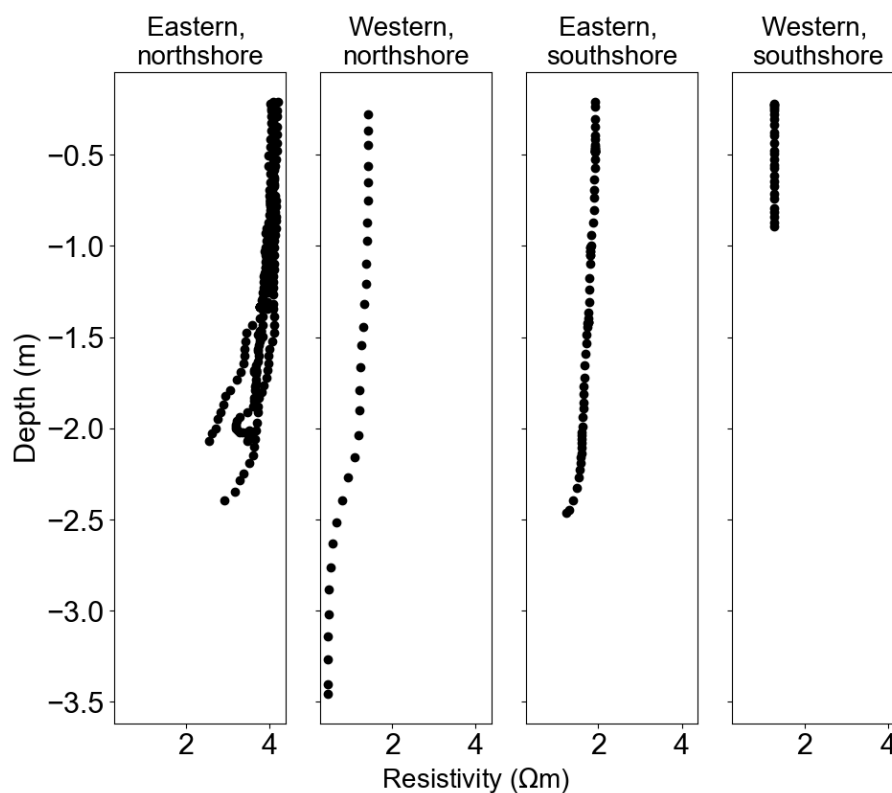
Figure A1. Water resistivity depth profiles from CTD measurements carried out on the respective ERT survey days
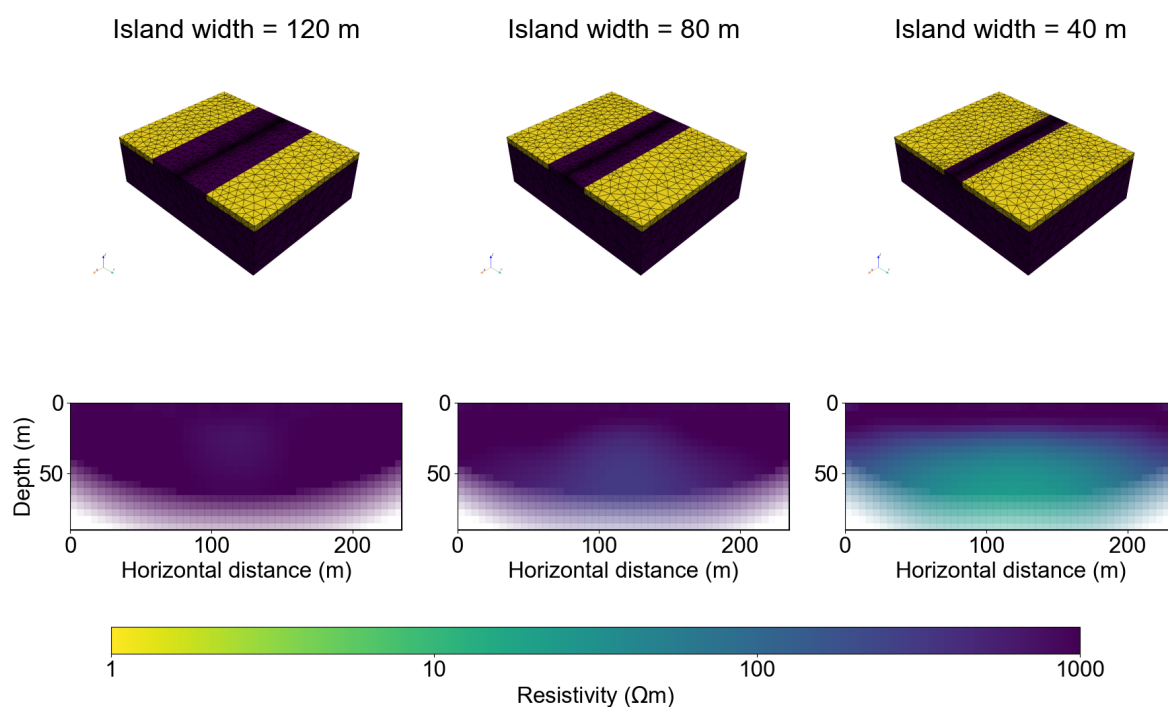
Figure A2. 3D forward modelling geometry (top row) and corresponding response cross-sections of the resistivity distribution (bottom row) for three synthetic scenarios with varying island widths: 120 m (left), 80 m (center), and 40 m (right). In the forwards model, the ground is assigned with a resistivity of 1000 Ωm (purple), and the seawater with a resistivity of 1 Ωm (yellow). The bottom panels show resistivity values along a horizontal transect beneath the island, with increasing island narrowness leading to reduced depth and lateral extent of resistivity anomalies.
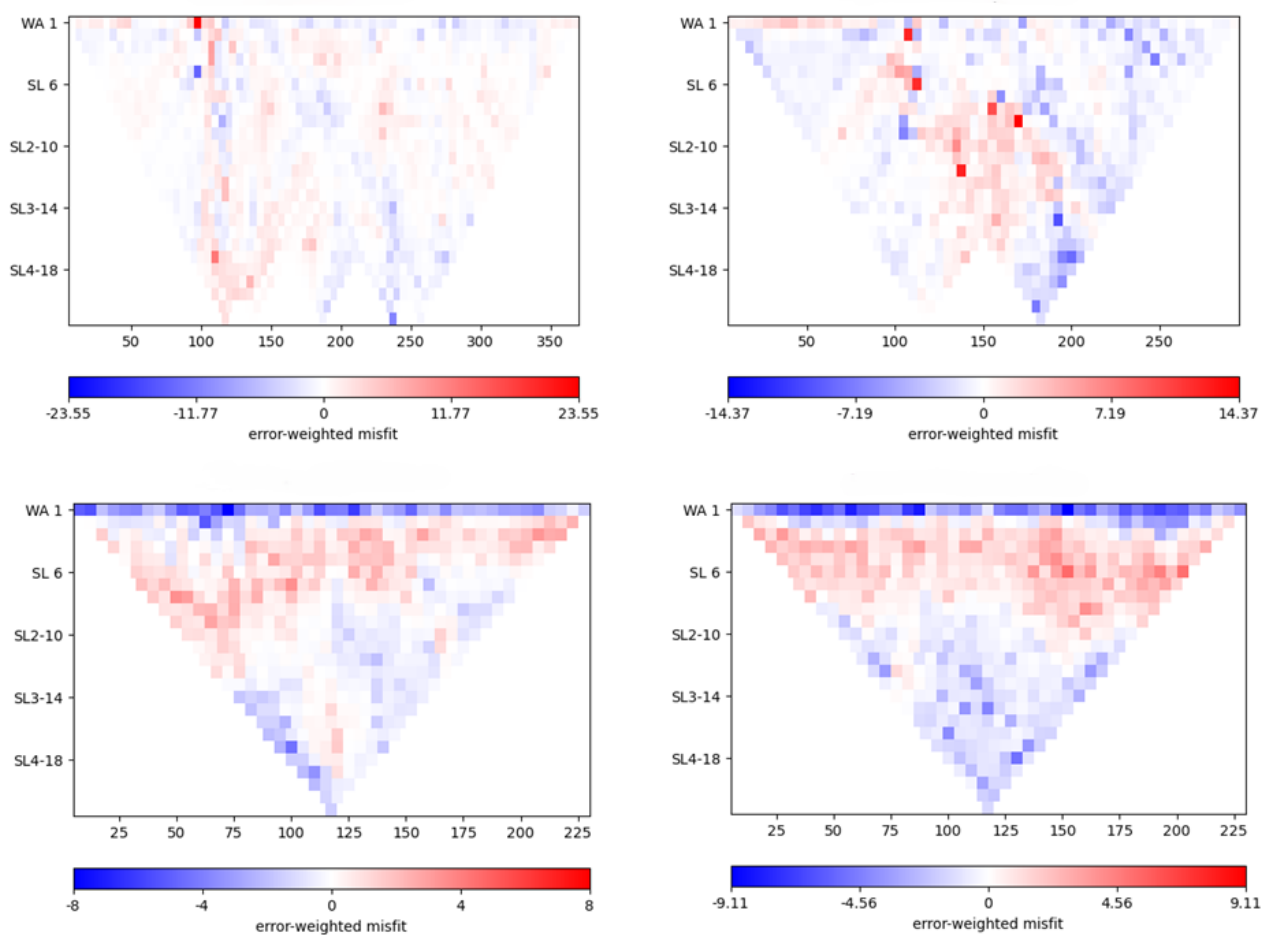
Figure A3. Error-weighted misfit distributions plotted in a pseudosection matrix. Panels show: (a) Eastern amphibious, (b) Western amphibious, (c) Eastern perpendicular, and (d) Western perpendicular profiles. The y-axis represents array types and spacings, with WA indicating Wenner-Alpha and SL indicating Schlumberger arrays with increasing electrode separation. The x-axis corresponds to data points ordered by acquisition geometry (reciprocal pairs). Colour scale indicates the magnitude and sign of the error-weighted misfit: blue for negative, red for positive, and white for well-fit data.
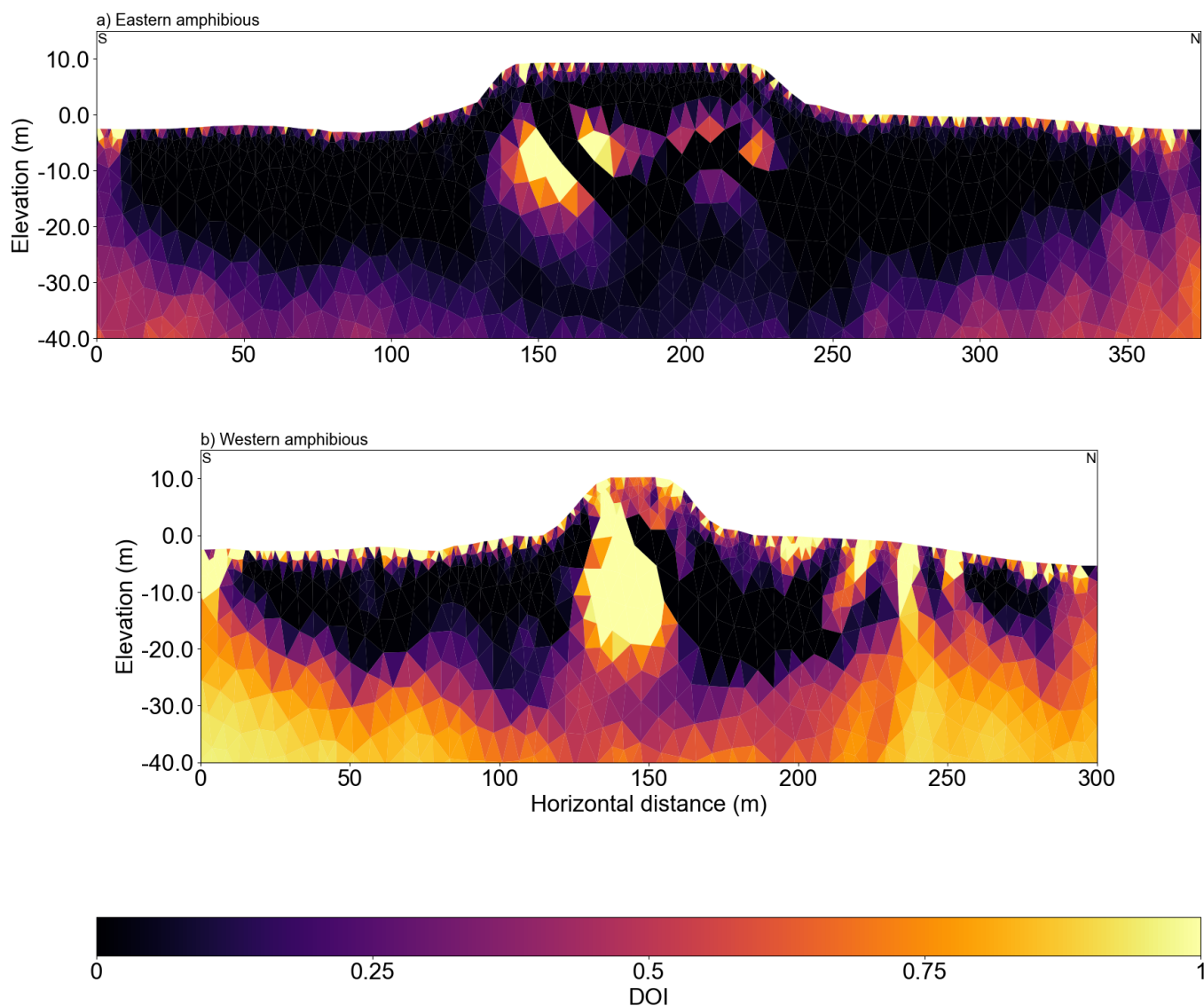
Figure A4. DOI sections for (a) the Eastern amphibious profile and (b) the Western amphibious profile. The DOI index is derived by comparing inversion results using different homogeneous reference models and reflects the sensitivity of the data to subsurface resistivity variations. Darker regions (low DOI values) indicate well-constrained areas where the inversion is less influenced by the choice of reference model and thus considered more reliable. Brighter regions (high DOI values) indicate lower sensitivity and greater dependence on the reference model.
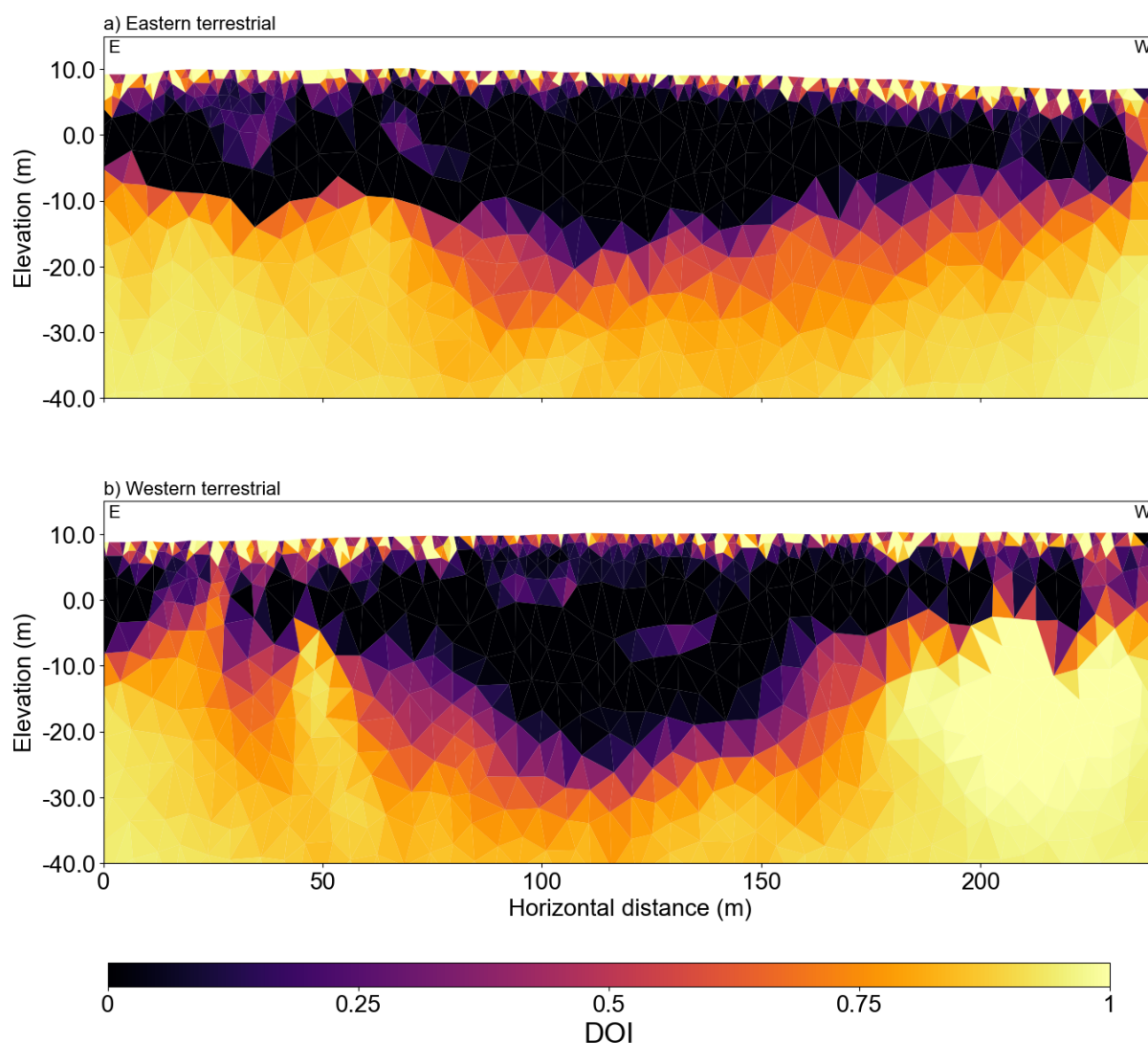
Figure A5. DOI sections for (a) the Eastern terrestrial profile and (b) the Western terrestrial profile. The DOI index is derived by comparing inversion results using different homogeneous reference models and reflects the sensitivity of the data to subsurface resistivity variations. Darker regions (low DOI values) indicate well-constrained areas where the inversion is less influenced by the choice of reference model and thus considered more reliable. Brighter regions (high DOI values) indicate lower sensitivity and greater dependence on the reference model.

745 *Author contributions.* This study was conceptualized and the methodology developed by MAl, MAn and PPO. Field work was carried out by MAn and PPO. MAl led the formal analysis and writing. All authors participated in creating, reviewing and editing the paper. Visualization was led by MAl with contributions from all co-authors. Funding was acquired by JB, PPO, and ML. All authors have read and agreed to the published version of the manuscript.

Competing interests. The authors declare no conflicts of interest.

750 *Acknowledgements.* We are grateful to Caroline Duchesne (NRCAN) for providing access to ground temperature data. James Keevik and Larry Lucas of Tuktoyaktuk provided expert assistance on the water. We thank Bennet Juhls for recovery and redeployment of bottom moorings in 2024. Trond Ryberg and Christian Haberland were of indispensable aid in the field. We are grateful to Thomas Günther and Nico Skibbe for their valuable advice on the pyGIMLI inversions. This study received funding from the European Union's Horizon Program through the projects Nunataryuk (grant agreement no. 773421), ILLUQ (grant agreement no. 101133587) and the Helmholtz Association
755 MOSES (Modular Observation Solutions for Earth Systems) project. MAl's position was partially funded through the AWI INSPIRES programme. MAn acknowledges funding from the DFG (project no. 533950637). ML acknowledges the project ThinIce (grant number 03F0943A) funded by Bundesministerium für Bildung und Forschung (BMBF).